# Cosmology with the *Roman Space Telescope* – multiprobe strategies

Tim Eifler [1]⋆ Hironao Miyatake [2,3,4,5] Elisabeth Krause,[1,6] Chen Heinrich,[2] Vivian Miranda,[1] Christopher Hirata,[7] Jiachuan Xu,[1] Shoubaneh Hemmati,[3] Melanie Simet,[2,8] Peter Capak,[9] Ami Choi,[7] Olivier Doré,[2,10] Cyrille Doux [11] Xiao Fang [1] Rebekah Hounsell,[12,13] Eric Huff,[2] Hung-Jin Huang [1] Mike Jarvis,[11] Jeffrey Kruk,[13] Dan Masters,[2] Eduardo Rozo,[6] Dan Scolnic [14] David N. Spergel,[15,16] Michael Troxel [14] Anja von der Linden,[17] Yun Wang,[9] David H. Weinberg,[7] Lukas Wenzl[18] and Hao-Yi Wu[7]

[1]*Department of Astronomy/Steward Observatory, University of Arizona, 933 North Cherry Avenue, Tucson, AZ 85721-0065, USA*
[2]*Jet Propulsion Laboratory, California Institute of Technology, Pasadena, CA 91109, USA*
[3]*Institute for Advanced Research, Nagoya University, Nagoya 464-8601, Japan*
[4]*Division of Physics and Astrophysical Science, Graduate School of Science, Nagoya University, Nagoya 464-8602, Japan*
[5]*Kavli IPMU (WPI), UTIAS, The University of Tokyo, Chiba 277-8583, Japan*
[6]*Department of Physics, University of Arizona, 1118 E Fourth Str, Tucson, AZ 85721, USA*
[7]*Center for Cosmology and AstroParticle Physics, The Ohio State University, 191 West Woodruff Avenue, Columbus, OH 43210, USA*
[8]*University of California Riverside, 900 University Ave, Riverside, CA 92521, USA*
[9]*IPAC, California Institute of Technology, Pasadena, CA 91125, USA*
[10]*California Institute of Technology, 1200 E. California Blvd, Pasadena, CA 91125, USA*
[11]*Department of Physics and Astronomy, University of Pennsylvania, Philadelphia, PA 19104, USA*
[12]*University of Maryland, Baltimore County, Baltimore, MD 21250, USA*
[13]*NASA Goddard Space Flight Center, Greenbelt, MD 20771, USA*
[14]*Department of Physics, Duke University, Durham, NC 27708, USA*
[15]*Center for Computational Astrophysics, Flatiron Institute, New York, NY 10010, USA*
[16]*Department of Astrophysical Sciences, Princeton University, Princeton, NJ 08544, USA*
[17]*Department of Physics and Astronomy, Stony Brook University, Stony Brook, NY 11794, USA*
[18]*Department of Astronomy, Cornell University, Ithaca, NY 14853, USA*

## ABSTRACT

We simulate the scientific performance of the Nancy Grace *Roman Space Telescope* High Latitude Survey (HLS) on dark energy and modified gravity. The 1.6-yr HLS Reference survey is currently envisioned to image 2000 deg$^2$ in multiple bands to a depth of ∼26.5 in *Y*, *J*, *H* and to cover the same area with slit-less spectroscopy beyond $z = 3$. The combination of deep, multiband photometry and deep spectroscopy will allow scientists to measure the growth and geometry of the Universe through a variety of cosmological probes (e.g. weak lensing, galaxy clusters, galaxy clustering, BAO, Type Ia supernova) and, equally, it will allow an exquisite control of observational and astrophysical systematic effects. In this paper, we explore multiprobe strategies that can be implemented, given the telescope's instrument capabilities. We model cosmological probes individually and jointly and account for correlated systematics and statistical uncertainties due to the higher order moments of the density field. We explore different levels of observational systematics for the HLS survey (photo-*z* and shear calibration) and ultimately run a joint likelihood analysis in *N*-dim parameter space. We find that the HLS reference survey alone can achieve a standard dark energy FoM of >300 when including all probes. This assumes no information from external data sets, we assume a flat universe however, and includes realistic assumptions for systematics. Our study of the HLS reference survey should be seen as part of a future community-driven effort to simulate and optimize the science return of the *Roman Space Telescope*.

**Key words:** cosmological parameters – cosmology: theory – large-scale structure of the Universe.

## 1 INTRODUCTION

In the current Lamda cold dark matter (ΛCDM) paradigm cosmic acceleration is caused by the Λ-term in the Einstein field equations (Einstein 1917). In terms of physical interpretation, Λ can be associated with the Universe's geometry or it can describe a new energy component of the universe, so-called dark energy. In 1998, two teams (Riess et al. 1998; Perlmutter et al. 1999) measured the energy density of Λ, $\Omega_\Lambda$, to be consistent with a value close to 0.7. To date, the science community lacks a convincing physics model for cosmic acceleration; constraining its properties and testing it against

⋆ E-mail: timeifler@gmail.com

alternative theories is one of the main science drivers of ongoing and future surveys.

Major progress on this topic is made by the current (Stage 3) generation of photometric surveys, such as Kilo-Degree Survey (KiDS[1]), the Hyper Suprime Cam (HSC[2]), the Dark Energy Survey (DES[3]), and spectroscopic surveys, such as the Baryon Oscillation Spectroscopic Survey (BOSS[4]). These low-redshift constraints of the ($\Lambda$CDM) model can be contrasted with cosmic microwave background (CMB) measurements from the early Universe made e.g. by the *Planck*[5] satellite, the Atacama Cosmology Telescope (ACT[6]), and the South Pole Telescope (SPT[7]). An emerging tension between these high- and low-redshift ($\Lambda$CDM) constraints may be indicative of new physics.

The potential tension between measurements, and with it the probability to discover new physics, increases with decreasing statistical uncertainty and better systematics control. With the advent of so-called Stage 4 surveys, e.g. the Dark Energy Spectroscopic Instrument (DESI; DESI Collaboration et al. 2016), the Prime Focus Spectrograph (PFS; Takada et al. 2014), the Large Synoptic Survey Telescope (LSST;[8] Ivezić et al. 2019), *Euclid*[9] (Laureijs et al. 2011), the Spectro-Photometer for the History of the Universe, Epoch of Reionization, and Ices Explorer (SPHEREx;[10] Doré et al. 2014), and the 4-metre MultiObject Spectroscopic Telescope (4MOST; de Jong 2019), the science community can expect an abundance of data to study the late-time Universe at increased precision. Similarly, the next generation of CMB surveys, such as the Simons Observatory (SO; Ade et al. 2019) and CMB-S4 (Abazajian et al. 2016) will enable us to contrast high and low redshift at increased precision and to combine information from both eras to increase the constraining power on cosmological models.

The *Roman Space Telescope*[11] (Spergel et al. 2015) is a successor mission to NASA's ground-breaking telescope endeavors such as the *Hubble Space Telescope* (*HST*[12]), the *Spitzer Space Telescope*,[13] and in the near future the *James Webb Space Telescope* (*JWST*[14]). The *Roman Space Telescope*'s science portfolio ranges from exoplanets to astrophysics to cosmology, building on a variety of standalone survey components: a microlensing survey, direct imaging of exoplanets, a supernovae (SNe) survey, a guest observer program, and the High Latitude Survey (HLS). The latter is the main focus of this paper; in particular, we aim to quantify the HLS' constraining power on physics driving the late-time accelerated expansion of the Universe through a combination of multiband imaging and spectroscopy.

The *Roman Space Telescope* is designed as a highly versatile missions that can flexibly react to findings of the aforementioned surveys. Its launch is planned for the mid-2020s into an L2 orbit with a nominal mission length of 5 yr; however, this primary survey can be extended given that there are no consumables that prevent a
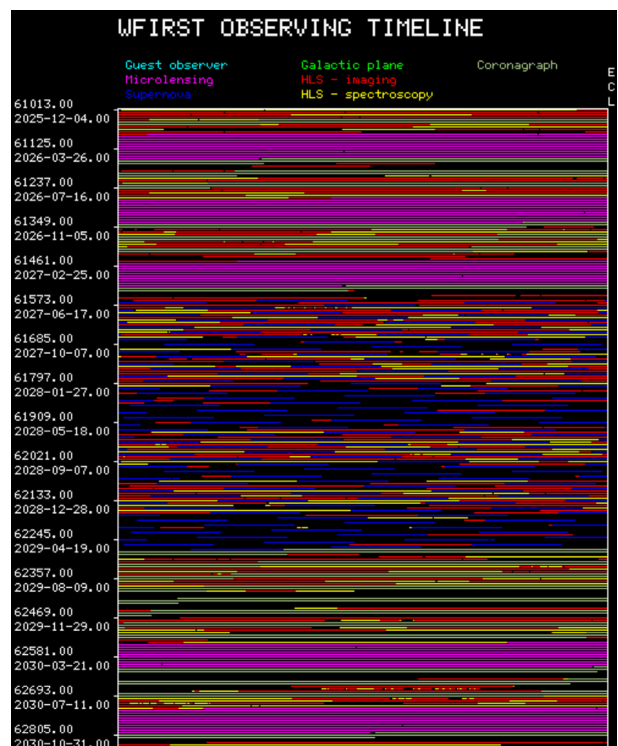
[1] http://www.astro-wise.org/projects/KIDS/

[2] http://www.naoj.org/Projects/HSC/HSCProject.html

[3] http://www.darkenergysurvey.org/

[4] http://www.sdss3.org/surveys/boss.php

[5] https://sci.esa.int/web/planck

[6] https://act.princeton.edu/

[7] https://pole.uchicago.edu/

[8] https://www.lsst.org/

[9] https://sci.esa.int/web/euclid

[10] http://spherex.caltech.edu/

[11] https://roman.gsfc.nasa.gov/

[12] https://hubblesite.org/

[13] http://www.spitzer.caltech.edu/

[14] https://www.jwst.nasa.gov/

**Figure 1.** An example *Roman Space Telescope* survey strategy as taken from the SDT 2015 report (Spergel et al. 2015) and computed from the exposure time calculator (ETC v0.13; Hirata et al. 2012). The individual survey components are colored into the timeline graphic: blue for the SN survey, magenta for microlensing, and red and yellow for the HLIS and HLSS, respectively. The remaining time will be allocated as guest observer proposals to the science community.

10+yr mission. The exact composition of the survey, i.e. the time allocation for the different science cases and the survey strategy within each science case is one of the most important topics that the community will discuss over the coming years prior to launch.

Fig. 1 shows an example *Roman Space Telescope* survey scenario composed of a 1.6-yr HLS, 6 months of SN observations distributed over 2 yr, an exoplanet and microlensing survey component, and a competed guest observer program that encompasses 25 per cent of the overall observing time. For the purpose of this paper we mainly focus on the HLS component, which can be divided further into the HLIS (High Latitude Imaging Survey) and the HLSS (High Latitude Spectroscopic Survey).

The reference survey of the *Roman Space Telescope* covers 2000 deg$^2$ with high-resolution, multiband photometric imaging in four near-infrared bands (HLIS) and deep grism spectroscopy (HLSS). This combination allows us to measure a variety of cosmological probes, e.g. weak lensing, photometric galaxy clustering, galaxy clusters, redshift space distortions (RSDs), and baryon acoustic oscillations (BAOs). Together with the SN survey, the reference HLS is designed to control systematics with minimal uncertainties; it will place tight constraints on the expansion history and structure growth in the Universe addressing questions about the nature of cosmic acceleration, neutrino physics, modified gravity, and dark matter.

In this paper, we develop a framework to simulate multiprobe strategies specifically for the *Roman Space Telescope*. We outline the top-level concepts of combining cosmological probes including inference and covariance implementation in Section 2, where we also

show the main results of the paper, i.e. the *Roman Space Telescope* forecast that includes weak lensing, galaxy–galaxy lensing, galaxy clustering (photometric and spectroscopic), galaxy clusters number counts, cluster weak lensing, and SN Ia. We consider subsets of this joint analysis and explore the impact of systematics in Sections 3–5. We conclude in Section 6.

## 2 MULTIPROBE LIKELIHOOD ANALYSES

Contrasting and subsequently combining multiple probes is one of the most promising avenues to constrain cosmology: Different probes are sensitive to different physics in the Universe, and they are affected differently by astrophysical uncertainties and observational systematics. Corresponding multiprobe strategies are relatively straightforward to implement if the observables are independent, e.g. when combining CMB temperature and polarization with BAO and SN Ia; however, the story is much more complex when combining correlated probes. In the latter case, one cannot simply combine the most sophisticated version of the single probe analyses a posteriori, but instead the analysis requires a joint covariances matrix that includes the statistical correlations and one must ensure the consistent modelling of systematics that affect the probes considered.

The *Roman Space Telescope*'s combination of spectroscopic and imaging instrumentation enables measuring a variety of LSS probes, such as weak lensing, galaxy clusters, galaxy clustering, and SN Ia. The latter can be treated as independent information, though SN magnification in overdense regions could become non-negligible at some point in the future. The other probes however are tracers of the same underlying density field, where modes are significantly correlated due to non-linear evolution of the late-time density field. A corresponding likelihood analysis requires a multiprobe covariance matrix.

### 2.1 Analysis choices

Designing a multiprobe analysis for the galaxies observed with the *Roman Space Telescope* reference survey can be broadly split into the following steps:

(i) *Choose broad categories of cosmological probes* that are to be combined: For our *Roman Space Telescope* reference survey, these are weak lensing, galaxy clusters, galaxy clustering (photometric and spectroscopic).

(ii) *Define specific probe combinations and summary statistics* that make up the data points of the data vector, which in our case are one-point functions and two-point functions that represent the corresponding probes. We do not consider higher-order correlation functions.

(iii) *Define the galaxy samples* that are associated with the aforementioned probes. We use the *Roman Space Telescope* ETC (Hirata et al. 2012) to compute realistic survey scenarios for the *Roman Space Telescope*'s coverage of area and depth in a given band. We fix the time per exposure and vary the number of exposures to build up depth over the survey area of a given scenario. For the HLS Reference Survey, this area is 2000 deg². The total survey time for a given number of exposures includes a simple prescription for overheads and is correct to approximately 10 per cent.

In order to obtain accurate redshift distributions, we closely follow Hemmati et al. (2019) in applying the ETC results to the CANDELS data set (Grogin et al. 2011; Koekemoer et al. 2011), which is the only data set available that is sufficiently deep in the near-infrared to model *Roman Space Telescope* observations. The ETC

has a built-in option to obtain a weak lensing catalogue based on an input catalogue of detected sources. The criteria for galaxies to be considered suitable for weak lensing are signal-to-noise ratio (S/N) > 18 ($J + H$ band combined, matched filter), ellipticity dispersion $\sigma_\epsilon$ < 0.2, and resolution factor $R > 0.4$, where we used the Bernstein & Jarvis (2002) convention (i.e. $\epsilon = (a^2 - b^2)/(a^2 + b^2)$ instead of $(a - b)/(a + b)$).

We apply these selections to the CANDELS catalogue and obtain our source sample for the HLS 4 NIR band survey. For the lens sample, we select CANDELS galaxies with S/N > 10 in each of the four HLS bands. Our *Roman Space Telescope* analysis assumes LSST photometry from the ground, hence we further down-select both samples by imposing an S/N > 5 cut in each LSST band except for the $u$ band (we note that 50 per cent of our galaxy sample has S/N > 5 in the $u$ band as well).

The resulting number densities for the HLS are

$$\bar{n}_{\text{source}} = N_{\text{source}}/\Omega_{\text{s}} = 51 \text{ galaxies arcmin}^{-2}, \tag{1}$$

$$\bar{n}_{\text{lens}} = N_{\text{lens}}/\Omega_{\text{s}} = 66 \text{ galaxies arcmin}^{-2}. \tag{2}$$

where $\Omega_{\text{s}}$ is the HLS reference survey area. We impose a $z_{\text{min}} = 0.25$ for the lens sample and define 10 tomographic bins for each sample such that $\bar{n}_x^i = \bar{n}_x/10$. These tomographic bins are then convolved with a Gaussian distribution, which is further described in Section 3.3.

We consider two different Gaussian photo-$z$ scenarios: an optimistic variation with mean zero and narrow width of $\sigma_z = 0.01$ and a more pessimistic scenario with broader kernel of $\sigma_z = 0.05$. The resulting redshift distributions are depicted in Fig. 2:

(a) *Source galaxy sample,* for which we require position, photometric redshift, and galaxy shape measurements.

(b) *Lens galaxy sample,* for which we require position and photometric redshift measurements.

(c) *Galaxy clusters,* for which we require position, photometric redshift, and optical richness estimates for galaxy clusters that are identified in the overall galaxy catalogue.

(d) *Spectroscopic galaxy sample,* which requires measurements of positions and spectroscopic redshifts.

(iv) *Define exact analysis choices.* Given that we are looking at two-point functions as summary statistics, we need to decide on the exact auto and cross-galaxy samples that constitute a cosmological probe. Further, we need to define the exact binning within each probe, in particular which angular scales and tomographic redshift binning are considered. The decision tree for these choices is complex and takes into account our ability to accurately model physics and systematics at specific angular scales and redshifts, and in particular our ability to model the correlations across all data points in the covariance matrix. For the data vector that we use to simulate the HLS reference Survey, we choose the follows:

(a) *Source galaxies – cosmic shear:* In terms of angular binning, we universally choose 25 logarithmically spaced Fourier mode bins ranging from $l_{\text{min}} = 30$ to $l_{\text{max}} = 15\,000$ for all two-point functions in our data vector; however, we impose different scale cuts for the different probes. The idea of universal binning across probes is driven by the desire to avoid computing cross-covariances of probes with different $l$-binning. For the cosmic shear part of the data vector we impose a scale cut of $l_{\text{max}}$(cosmic shear) = 4000, which leaves 20 bins that carry information. The ten tomographic bins translate into 55 auto and cross-power spectra.
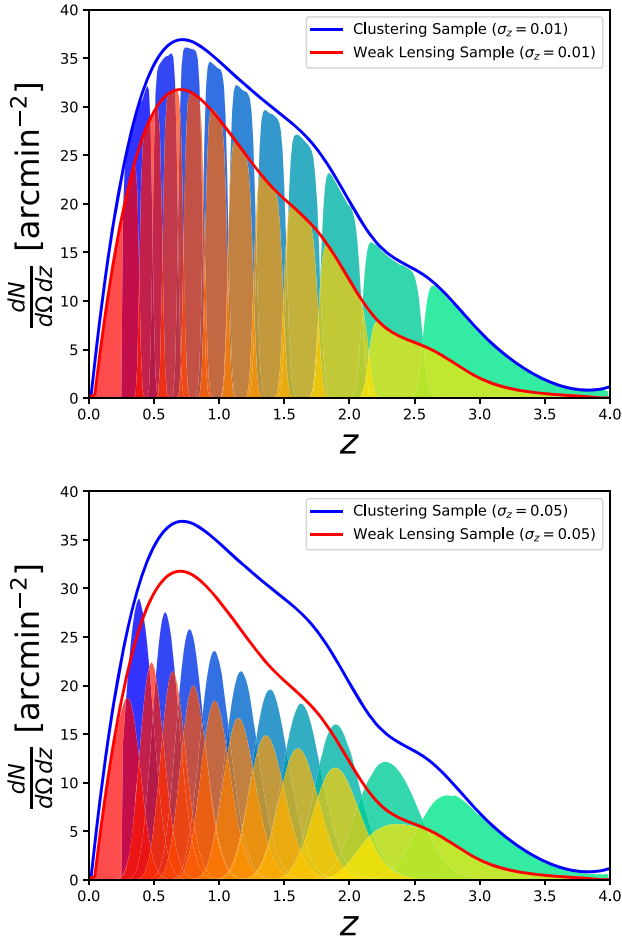
**Figure 2.** The redshift distributions for the lens and source galaxy sample for two different levels of photometric redshift precision, $\sigma_z = 0.01$ and $0.05$, respectively. These map on to our optimistic and pessimistic systematics scenarios considered for the HLIS.

(b) *Lens galaxies – photometric clustering:* The redshift distribution for the lens sample is further detailed in Section 3.3 and divided into 10 tomographic bins. We exclude *l*-bins, if scales below $R_{min} = 2\pi/k_{max} = 21$ Mpc $h^{-1}$ contribute to the Limber integral (see equation 5), which imposes a redshift-dependent scale cut in the *l*-binning.

(c) *Lens × source galaxies – photometric galaxy-galaxy lensing:* The galaxy–galaxy lensing part of the data vector assumes the lens galaxy sample as foreground and the source galaxy sample as background galaxies; we only consider source–lens combinations where the source bin is fully behind the lens bin in redshift. We again impose a cut-off at $R_{min} = 21$ Mpc $h^{-1}$.

(d) *Galaxy cluster number counts:* This is the one-point function we include in our data vector. We split our cluster sample into four cluster redshift bins (0.4–0.6, 0.6–0.8, 0.8–1.0, 1.0–1.2) and four cluster richness bins between $\lambda_{min} = 40$ and $\lambda_{max} = 220$ in each redshift bin.

(e) *Galaxy clusters × source galaxies – cluster weak lensing:* In order to calibrate the cluster mass–richness relation (equation 26), we consider the stacked weak lensing signal from all combinations of cluster redshift and richness bins with source galaxies, with the restriction that source galaxies are located

at higher redshift than the galaxy clusters. Specifically, we use the cluster lensing power spectrum in the angular range $4000 < l < 15\,000$, which corresponds mostly to the one-halo cluster lensing signal.

(f) *Spectroscopic × spectroscopic – spectroscopic galaxy clustering:* While our analysis considers all cross-covariance terms for the five cosmological probes above, the *Roman Space Telescope*'s spectroscopic clustering is treated as an independent probe whose cosmological information is determined separately and added a posteriori. This is an approximation; however, the derivation of a 2D + 3D joint covariance is beyond the scope of this paper and deferred to future work. Our spectroscopic clustering data vector is comprised of 3D power spectrum Fourier modes $P(k, \mu)$ and we select 100 logarithmic bins ranging from $k_{min} = 0.001$ to $k_{max} = 0.3\,h\,\mathrm{Mpc}^{-1}$, 10 linearly spaced $\mu$ bins from 0 to 1.0, and 7 density-weighted redshift bins that start at 0.83 and range out to 3.7. This data vector captures both the BAO and RSD information.

### 2.2 Inference, likelihoods, covariances

Given the data vector $\boldsymbol{D}$, we sample the joint parameter space of cosmological $\boldsymbol{p}_c$ and nuisance parameters $\boldsymbol{p}_n$ using the EMCEE[15] (Foreman-Mackey et al. 2013), which is based on the affine-invariant sampler of Goodman & Weare (2010). At each step, we compute the posterior using Bayes' theorem:

$$P(\boldsymbol{p}_c, \boldsymbol{p}_n | \boldsymbol{D}) \propto \underbrace{P_r(\boldsymbol{p}_c, \boldsymbol{p}_n)}_{\text{SN Ia}} \underbrace{L(\boldsymbol{D}|\boldsymbol{p}_c, \boldsymbol{p}_n)}_{\text{HLS}}. \quad (3)$$

$P_r(\boldsymbol{p}_c, \boldsymbol{p}_n)$ denotes the prior probability, which, in our case, is based on the *Roman Space Telescope* SN Ia survey forecast from (Hounsell et al. 2018). Specifically, we reran the 'Imaging: Allz (optimistic)' scenario (cf. section 5.4 and table 13 in Hounsell et al. 2018) centred it on the fiducial cosmology of our analysis. We did not include any information from CMB or BAO experiments, which explains the different contours compared to Hounsell et al. (2018).

The cosmological information from the HLS enters our simulations through the second term in equation (3), i.e. the likelihood, $L(\boldsymbol{D}|\boldsymbol{p}_c, \boldsymbol{p}_n) = N \times \exp(-(1/2)\chi^2(\boldsymbol{p}_c, \boldsymbol{p}_n))$. We assume that the errors of this data vector are distributed as a multivariate Gaussian:

$$L(\boldsymbol{D}, \boldsymbol{p}_c, \boldsymbol{p}_n) = N \times \exp\left(-\frac{1}{2}\left[\chi^2_{\text{HLIS}}(\boldsymbol{p}_c, \boldsymbol{p}_n) + \chi^2_{\text{HLSS}}(\boldsymbol{p}_c, \boldsymbol{p}_n)\right]\right), \quad (4)$$

which is composed of two $\chi^2 = (\boldsymbol{D} - \boldsymbol{M})^t\,\mathbf{C}^{-1}\,(\boldsymbol{D} - \boldsymbol{M})$ terms reflecting our approximation that the cosmological information from HLSS and HLIS is independent. We note that future work should explore correlations between HLIS and HLSS and develop a joint covariance matrix for these measurements. $N$ is a normalization constant.

Based on the analysis choices (probes, redshifts, scales) described in Section 2.1 we compute the data vectors and covariance matrices for HLIS and HLSS at the fiducial cosmology and systematics parameters (see Tables 2, 5 and 7 for the different probes). In case of the HLSS survey the covariance matrix is diagonal and further described in Section 5, in case of the HLIS, the matrix has significant off-diagonal terms (see Fig. 3).

Fig. 3 illustrates the structure of the matrix with the autoprobe matrices denoted as numbers 1–5 corresponding to cosmic shear (1),
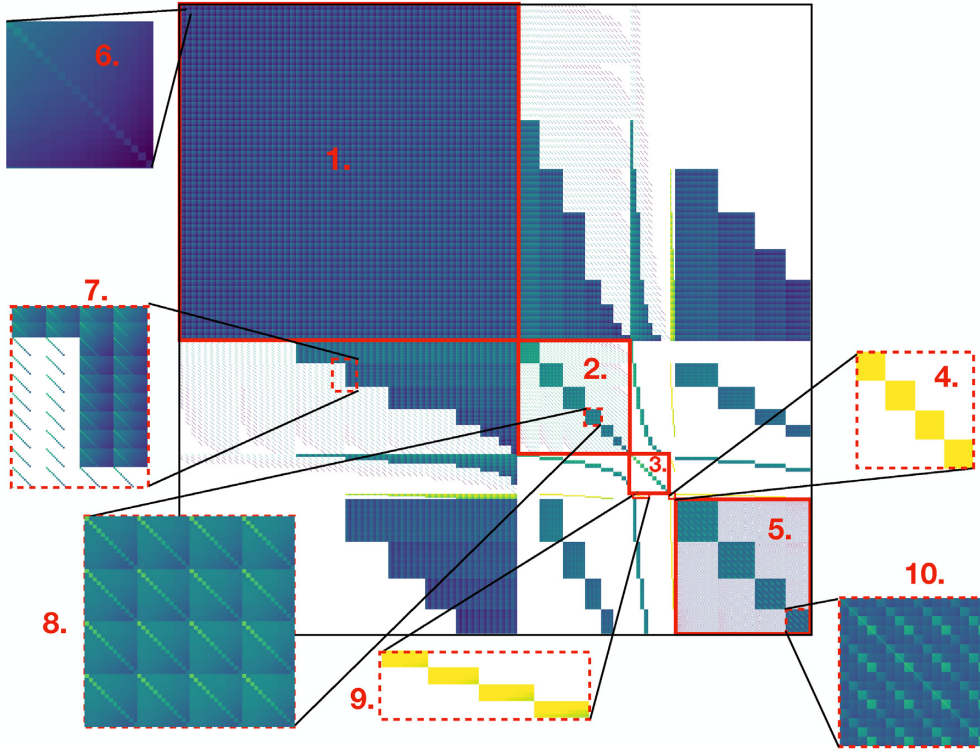
[15]https://emcee.readthedocs.io/en/stable/

**Figure 3.** The multiprobe covariance matrix for the HLIS survey, calculated under the Limber approximation, where we have highlighted some parts of the matrix to illustrate the correlation structure: (1) depicts the cosmic shear covariance matrix, comprised of 55 tomographic combinations of source bins, each with 20 fourier *l*-bins. (5) shows one of the tomographic combinations, and the individual $l_1$, $l_2$ elements are clearly visible. (2) is the galaxy–galaxy lensing tomography covariance with (8) being the galaxy–galaxy combinations of the fourth lens bin with all the non-overlapping source bins at higher redshifts. (3) is the clustering autoprobe matrix with 10 tomographic bins. (4) corresponds to the cluster number counts autoprobe matrix, which is comprised of four cluster redshift bins each with four richness bins (hardly distinguishable within in the four yellow squares). (5) is the autoprobe covariance of the cluster weak lensing part of the data vector, which uses the four cluster redshift bins as lens bins and the source sample as source bins. (10) zooms into the covariance of the fourth cluster redshift bin, which again is split into four richness bins, all of which are then correlated with the highest four source galaxy redshift bins. One can see that the diagonal structure consists of 16 blocks that are each composed of 5×5 elements. The latter correspond to the covariance of the five cluster weak lensing *l*-bins, which range from $l \in [4000\text{–}15\,000]$. Zoom-in box (6) is a zoom into the first tomographic bin combination cosmic shear covariance matrix, and (7) shows the cross-probe covariance of cosmic shear and galaxy–galaxy lensing. The impact of the $k_{max}$ scale cuts causes the blocks to be non-quadratic. The Limber approximation leads to non-Gaussian terms only for specific combinations of lens and source tomographic bins (all three source bins need to be behind the lens bin). (9) is the cross-probe covariance of galaxy clustering and cluster number counts, which only has non-zero elements when both probes overlap in redshift, i.e. in the range $z \in [0.2\text{–}1.2]$. The shape of the yellow rectangles is determined by the number of *l*-bins used in the clustering data vector, i.e. 20, and the number of richness bins in cluster number counts, i.e. four.

galaxy–galaxy lensing (2), photometric galaxy clustering (3), cluster number counts (4), and cluster weak lensing (5). Calculation of the individual terms of the covariance can be found in the Appendix (equations A2–A14 of Krause & Eifler 2017).

Since this covariance matrix is calculated analytically and not estimated from either simulations or data, it can be considered noise-free and is easily invertible. It does not inherently limit the number of data points that can enter our analysis, which would be the case if the covariance were computed from a limited set of realizations (see e.g. Taylor, Joachimi & Kitching 2013; Dodelson & Schneider 2013, for details on these constraints).

We compute figures of merit (FoMs) from the parameter covariance extracted from the MCMC chains. We note that for highly non-Gaussian posteriors this process will not accurately map constraining power. Given the parameter covariance, we compute the FoM = $[\det \mathbf{C}(p_1, p_2)]^{-1/2}$. In almost all cases in this paper ($p_1$, $p_2$) = ($w_0$, $w_a$), which makes it consistent with the well-known dark energy FoM; however, when considering the modified gravity FoM, we use the modified gravity parameters ($p_1$, $p_2$) = ($\mu$, $\Sigma$). The FoMs

for the multiprobe analysis depicted in Fig. 4 can be found in Table 1; all likelihood settings are summarized in Table 2.

## 3 COSMIC SHEAR AND GALAXY CLUSTERING

We start exploring the *Roman Space Telescope* multiprobe analyses by looking at the HLIS weak lensing and photometric galaxy clustering probes, which when combined with galaxy–galaxy lensing form a so-called 3×2pt analysis. Here, we summarize the computation of angular (cross-)power spectra for the different probes and the computation of galaxy cluster number counts. We use capital Roman subscripts to denote observables, $A$, $B \in \{\kappa, \delta_g, \delta_{\lambda_\alpha}\}$, where $\kappa$ references lensing, and $\delta_g$ is the density contrast of (lens) galaxies. The density contrast of galaxy clusters in richness bin $\alpha$, $\delta_{\lambda_\alpha}$, will be considered in Section 4. The results for the 3x2 fiducial likelihood analyses are summarized in Fig. 5 and Table 3; a systematics study is shown in Fig. 6 and quantified in Table 4.
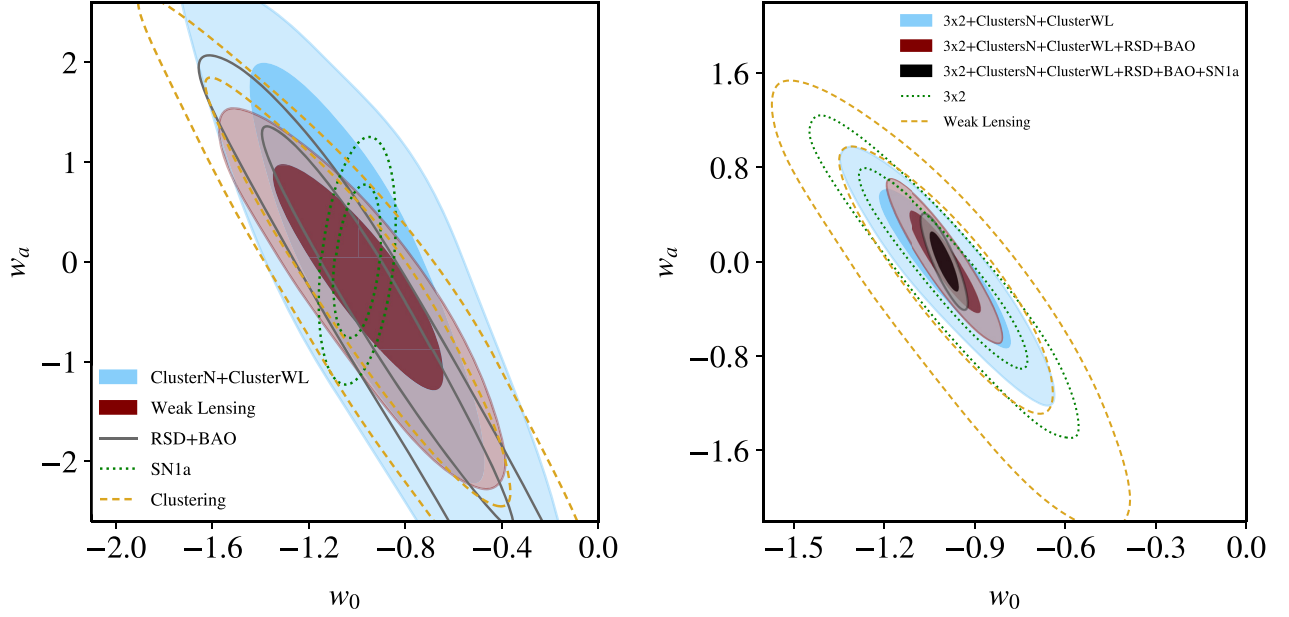
**Figure 4.** Left-hand panel: individual probes considered in this analysis, i.e. weak lensing, photometric galaxy clustering, galaxy cluster number counts calibrated through cluster weak lensing, RSD power spectra including the BAO scale, and SN Ia. Right-hand panel: multiprobe analyses starting from weak lensing only, then adding photometric clustering and galaxy–galaxy lensing (3×2), then adding cluster number counts and cluster weak lensing, then adding RSD and BAO information, and lastly adding in SN Ia based on the findings of (Hounsell et al. 2018). The FoMs for the individual and multiprobe chains can be found in Table 1.

**Table 1.** FoMs for individual and multiprobe chains depicted in Fig. 4.

| Probe | Multiprobe FoM summary | |
| --- | --- | --- |
| | Individual | Cumulative |
| Cosmic shear | 9.8 | 9.8 |
| 3×2 | 23.46 | 23.46 |
| Clusters | 3.86 | 31.56 |
| RSD + BAO | 8.19 | 89.54 |
| SN Ia | 24.62 | 300.11 |

*Notes.* Note that 3×2 includes cosmic shear. All FoMs assume a flat universe.

### 3.1 Modelling of observables

We calculate the angular power spectrum between redshift bin $i$ of observable $A$ and redshift bin $j$ of observables $B$ at projected Fourier mode $l$, $C_{AB}^{ij}(l)$, using the Limber and flat-sky approximations (we refer to e.g. Fang et al. 2019, for the potential impact when analysing data):

$$C_{AB}^{ij}(l) = \int d\chi \frac{q_A^i(\chi) q_B^j(\chi)}{\chi^2} P_{AB}(l/\chi, z(\chi)), \quad (5)$$

where $\chi$ is the comoving distance, $q_A^i(\chi)$ are weight functions of the different observables given in equations (6) and (7), and $P_{AB}(k, z)$ are the three-dimensional, probe-specific power spectra detailed below. The weight function for the projected galaxy density in redshift bin $i$, $q_{\delta_g}^i(\chi)$ is, given the normalized comoving distance probability of galaxies in this redshift bin,

$$q_{\delta_g}^i(\chi) = \frac{n_{lens}^i(z(\chi))}{\bar{n}_{lens}^i} \frac{dz}{d\chi}, \quad (6)$$

with $n_{lens}^i(z)$ the redshift distribution of galaxies in (photometric) galaxy redshift bin $i$ (cf. equation 17), and $\bar{n}_{lens}^i$ the angular number

densities of galaxies in this redshift bin (cf. equation 1). For the convergence field, the weight function $q_\kappa^i(\chi)$ is the lens efficiency,

$$q_\kappa^i(\chi) = \frac{3H_0^2 \Omega_m}{2c^2} \frac{\chi}{a(\chi)} \int_\chi^{\chi_h} d\chi' \frac{n_{source}^i(z(\chi'))dz/d\chi'}{\bar{n}_{source}^i} \frac{\chi' - \chi}{\chi'}, \quad (7)$$

with $n_{source}^i(z)$ the the redshift distribution of source galaxies in (photometric) source redshift bin $i$ (equation 17), $\bar{n}_{source}^i$ is the angular number densities of source galaxies in this redshift bin (equation 1), and $a(\chi)$ is the scale factor.

The three-dimensional power spectra $P_{AB}(k, z)$ can be expressed through the matter density power spectrum $P_{mm}(k, z)$. For the purpose of this section, $P_{mm}(k, z)$ corresponds to the density power spectrum $P_{\delta\delta}(k, z)$, where we use the Takahashi et al. (2012) fitting formula to model non-linear evolution. Noting that $P_{AB} = P_{BA}$, we describe the different cases in equations (8, 9, 23). For $A = \kappa$, this is trivial:

$$P_{\kappa B}(k, z) = P_{mB}(k, z). \quad (8)$$

For quantities related to the galaxy density, we note that we only consider the large-scale galaxy distribution, where it is valid to assume that the galaxy density contrast on these scales can be approximated as the non-linear matter density contrast times an effective galaxy bias parameter $b_g(z)$:

$$P_{\delta_g B}(k, z) = b_g(z) P_{mB}(k, z). \quad (9)$$

### 3.2 Modified gravity modelling

Since there is no compelling model of modified gravity, we adopt phenomenological modified gravity parameters $(\mu_0, \Sigma_0)$ that we define similar as e.g. Simpson et al. (2013).

In this parametrization the expressions for the Newtonian potential $\Psi$ and the curvature potential $\Phi$ that govern the perturbed

**Table 2.** Fiducial parameters, flat priors (min, max) for cosmology and galaxy bias, and Gaussian priors ($\mu$, $\sigma$) for observational systematics.

| Parameter | Fiducial | Prior |
|---|---|---|
| | **Survey** | |
| $\Omega_s$ | 2000 deg$^2$ | Fixed |
| $n_{source}$ | 51 galaxies arcmin$^{-2}$ | Fixed |
| $n_{lens}$ | 66 galaxies arcmin$^{-2}$ | Fixed |
| $\sigma_\epsilon$ | 0.26 | Fixed |
| | **Cosmology** | |
| $\Omega_m$ | 0.3156 | Flat (0.1, 0.6) |
| $\sigma_8$ | 0.831 | Flat (0.6, 0.95) |
| $n_s$ | 0.9645 | Flat (0.85, 1.06) |
| $w_0$ | −1.0 | Flat (−2.0, 0.0) |
| $w_a$ | 0.0 | Flat (−2.5, 2.5) |
| $\Omega_b$ | 0.0492 | Flat (0.04, 0.055) |
| $h_0$ | 0.6727 | Flat (0.6, 0.76) |
| | **Galaxy bias (tomographic bins)** | |
| $b_g^i$ | $1.3 + i \times 0.1$ | Flat (0.8, 3.0) |
| | **Lens photo-$z$ (optimistic)** | |
| $\Delta_{z,lens}^i$ | 0.0 | Gauss (0.0, 0.002) |
| $\sigma_{z,\,lens}$ | 0.01 | Gauss (0.01, 0.002) |
| | **Lens photo-$z$ (pessimistic)** | |
| $\Delta_{z,lens}^i$ | 0.0 | Gauss (0.0, 0.02) |
| $\sigma_{z,\,lens}$ | 0.05 | Gauss (0.05, 0.02) |
| | **Source photo-$z$ (optimistic)** | |
| $\Delta_{z,source}^i$ | 0.0 | Gauss (0.0, 0.002) |
| $\sigma_{z,\,source}$ | 0.01 | Gauss (0.01, 0.002) |
| | **Source photo-$z$ (pessimistic)** | |
| $\Delta_{z,source}^i$ | 0.0 | Gauss (0.0, 0.02) |
| $\sigma_{z,\,source}$ | 0.05 | Gauss (0.05, 0.02) |
| | **Shear calibration (optimistic)** | |
| $m_i$ | 0.0 | Gauss (0.0, 0.002) |
| | **Shear calibration (pessimistic)** | |
| $m_i$ | 0.0 | Gauss (0.0, 0.01) |

*Notes.* We consider optimistic and pessimistic scenarios in this paper, which is indicated in the corresponding sections of the table. The ellipticity dispersion value is for one ellipticity component.

Friedmann–Robertson–Walker metric,

$$ds^2 = (1 + 2\Psi)dt^2 - a^2(t)(1 - 2\Phi)dx^2, \tag{10}$$

are altered. Within general relativity $\Psi = \Phi$ holds. The ($\mu$, $\Sigma$) parameters give additional freedom to the Newtonian gravitational potential $\Psi$ experienced by non-relativistic particles and the lensing potential ($\Phi + \Psi$) experienced by relativistic particles, specifically

$$\Psi(k, a) = [1 + \mu(a)]\Psi_{GR}(k, a), \tag{11}$$

$$\Psi(k, a) + \Phi(k, a) = [1 + \Sigma(a)](\Psi_{GR}(k, a) + \Phi_{GR}(k, a)). \tag{12}$$

We assume that $\mu(a)$ and $\Sigma(a)$ are both scale independent. Furthermore, since their motivation was to explain the dark energy phenomenon, we assume that the modified gravity parameters scale with the dark energy density, i.e.

$$\mu(a) = \mu_0 \frac{\Omega_\Lambda(a)}{\Omega_\Lambda}, \tag{13}$$

$$\Sigma(a) = \Sigma_0 \frac{\Omega_\Lambda(a)}{\Omega_\Lambda}, \tag{14}$$

where $\Omega_\Lambda$ is the present-day dark energy density. Note that in the case of general relativity, $\mu_0 = \Sigma_0 = 0$.

The $\mu_0$ parameter modifies the growth of linear density perturbation such that

$$\delta'' + \left(\frac{2}{a} + \frac{\ddot{a}}{\dot{a}^2}\right)\delta' - \frac{3\Omega_m}{2a^2}[1 + \mu(a)]\delta = 0, \tag{15}$$

which changes the growth function, and consequently the density–density power spectrum $P_{\delta\delta}$ and all projected power spectra described in equation (5).

The $\Sigma_0$ parameter only affects lensing related quantities, which in a 3×2pt analysis means the galaxy–shear and shear–shear power spectrum. Specifically, equation (5) is modified as

$$C_{AB}^{ij}(l) = \int d\chi \frac{q_A^i(\chi)q_B^j(\chi)}{\chi^2}[1 + \Sigma(\chi)]^k P_{AB}(l/\chi, z(\chi)), \tag{16}$$

where the exponent $k = 2$ if $A = B = \kappa$, $k = 0$ if $A = B = \delta_g$, and $k = 1$ if either $A = \kappa$ or $B = \kappa$.

### 3.3 Systematics

We parametrize uncertainties arising from systematics through nuisance parameters, which are summarized with their fiducial values and priors in Table 2. Our default likelihood analysis includes the following systematics:

#### 3.3.1 Photometric redshift uncertainties

The true redshift distribution as measured from the CANDELS data (cf. Fig. 2) is convolved with a Gaussian photometric redshift uncertainty model to obtain the distribution within tomographic bin $i$:

$$n_x^i(z_{ph}) = \int_{z_{min,x}^i}^{z_{max,x}^i} dz\, n_x(z)\, p^i\left(z_{ph}|z, x\right), \tag{17}$$

where $p(z_{ph}|z, x)$ is the probability distribution of $z_{ph}$ at given true redshift $z$ for galaxies from population $x$:

$$p^i\left(z_{ph}|z, x\right) = \frac{1}{\sqrt{2\pi}\sigma_{z,x}(1+z)}\exp\left[-\frac{\left(z - z_{ph} - \Delta_{z,x}^i\right)^2}{2\left(\sigma_{z,x}(1+z)\right)^2}\right]. \tag{18}$$

The resulting Gaussian tomographic bin is parametrized through scatter $\sigma_z(z)$ and bias between $z$ and $z_{ph}$, i.e. $\Delta_z^i(z)$. The bias $\Delta_z^i(z)$ has fiducial value of zero; the fiducial value for $\sigma_z$ is assumed to be the same for the lens and source sample and we choose $\sigma_z = 0.01$ for the optimistic and $\sigma_z = 0.05$ for the pessimistic scenario. The resulting distributions are shown in Fig. 2.

In this analysis we only consider Gaussian photometric redshift uncertainties, which are characterized by scatter $\sigma_z(z)$ and bias $\Delta_z(z)$. While these may in general be arbitrary functions, we further assume that the scatter can be described by the simple redshift scaling $\sigma_{z,x}(1 + z)$ and allow one (constant) bias parameter $\Delta_{z,x}^i$ per redshift bin. For our 10 lens and source galaxy redshift bins, this model results in 22 parameters describing photo-$z$ uncertainty, 10 photo-$z$ bias, and 1 photo-$z$ scatter parameter for each lens and source sample.

#### 3.3.2 Linear galaxy bias

Linear galaxy bias is described by one nuisance parameter per tomographic lens galaxy redshift bin, which is marginalized over using conservative flat priors in a likelihood analysis. The fiducial values of galaxy bias in lens bin $i$ follow the simple description $1.3 + i \times 0.1$. We note that the actual fiducial value is not important for the constraining power; important is the range over which we
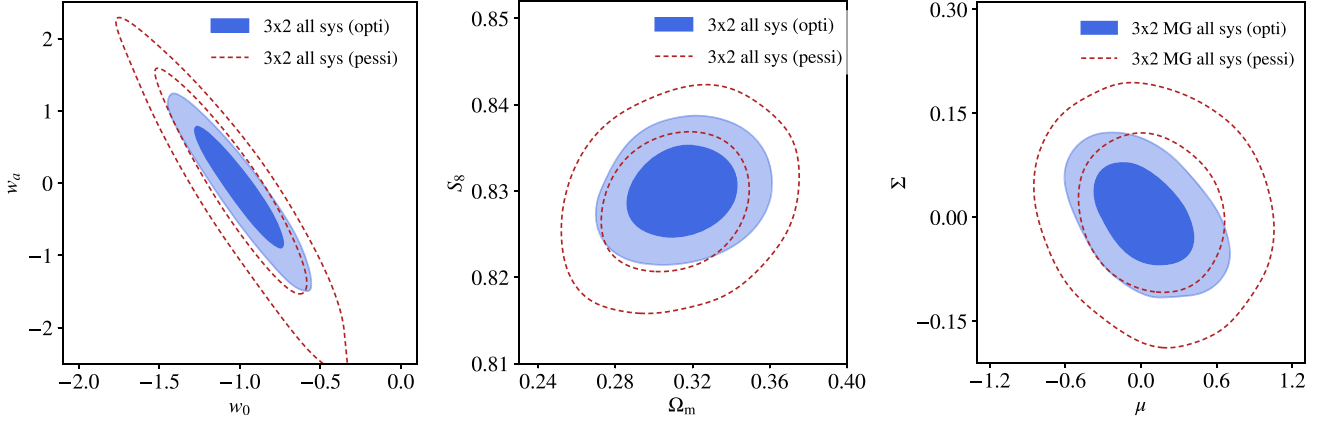
**Figure 5.** Constraining power on dark energy equation of state parameters $w_0$ and $w_a$ (left-hand panels), $\Omega_m$ and $S_8$ (middle panel), and on modified gravity parameters $\Sigma_0$ and $\mu_0$ for optimistic and pessimistic systematics scenarios for a 3×2 analysis. Note that the likelihood analysis in the two left-hand panels assume GR to be the correct theory, and only in the right-hand panels we vary $\Sigma_0$ and $\mu_0$. The relative loss in information depicted here is quantified as FoMs in Table 3.

**Table 3.** FoMs for optimistic and pessimistic systematics scenarios for the science cases depicted in Fig. 5.

| Science case | 3×2 different science cases FoM summary | |
|---|---|---|
| | Optimistic | Pessimistic |
| Dark energy | 23.46 | 7.88 |
| Modified gravity | 22.20 | 9.49 |

marginalize (flat priors from 0.8 to 3.0) and the fact that we use one free parameter per redshift bin instead of a parametrized redshift evolution.

Future efforts should investigate several aspects of galaxy bias: (1) perturbative or simulation based parametrizations that allow the analyst to push to smaller scales; (2) improved parametrizations, in particular such that parametrize the redshift evolution with fewer parameters; and (3) informative priors.

### 3.3.3 Multiplicative shear calibration

Multiplicative shear calibration is modeled using one parameter $m^i$ per redshift bin, which affects cosmic shear and galaxy–galaxy lensing power spectra via

$$
\begin{aligned}
C^{ij}_{\kappa\kappa}(l) &\longrightarrow (1 + m^i)(1 + m^j)\, C^{ij}_{\kappa\kappa}(l), \\
C^{ij}_{\delta_g\kappa}(l) &\longrightarrow (1 + m^j)\, C^{ij}_{\delta_g\kappa}(l),
\end{aligned}
\tag{19}
$$

where the cluster lensing power spectra are affected analogously to the galaxy–galaxy lensing spectra. We marginalize over each $m^i$ independently with Gaussian priors (10 parameters). Similar to the photo-$z$ scenarios we are looking at optimistic and pessimistic prior information shear calibration (which can come from either simulations or external data such as in Schaan et al. 2017).

### 3.3.4 Other systematics

In this paper, we only consider observational uncertainties (and galaxy bias), but neglect astrophysical systematics most notably baryonic physics uncertainties (e.g. Semboloni et al. 2011; van Daalen et al. 2011; Zentner et al. 2013; Eifler et al. 2015; Chisari

et al. 2018; Chisari et al. 2019; Huang et al. 2019) and uncertainties in modelling intrinsic alignment of galaxies (e.g. Hirata & Seljak 2004; Mandelbaum et al. 2006; Joachimi & Bridle 2010; Troxel & Ishak 2014; Blazek, Vlah & Seljak 2015; Chisari et al. 2015; Singh, Mandelbaum & More 2015; Tenneti et al. 2015; Krause, Eifler & Blazek 2016; Blazek et al. 2019; Samuroff et al. 2019; Vlah, Chisari & Schmidt 2019). We show results for optimistic and pessimistic scenarios for observational systematics in Fig. 6 and Table 4. In the context of 3×2pt analyses for the *Roman Space Telescope* and LSST, we explore the impact of baryonic physics and intrinsic alignment in a companion paper (Eifler et al. 2020).

## 4 GALAXY CLUSTERS

This section summarizes the halo model for galaxy cluster observables employed in this analysis. We consider galaxy clusters stacked in bins of optical richness, $\lambda_\alpha$, and relate their properties to dark matter haloes using the probability distribution function $p(\ln \lambda | M, z)$, which describes the probability that a dark matter halo of mass $M$ at redshift $z$ hosts a cluster with richness $\lambda$. We will specify and explain our specific choice of cluster mass–observable relation (MOR) further in Section 4.2. Throughout this paper, we define halo properties using the overdensity $\Delta = 200$, which is defined with respect to the mean matter density, and employ the Tinker et al. (2010) fitting function for the halo mass function.

### 4.1 Modelling of observables

#### 4.1.1 Cluster number counts

The expected cluster count in richness bin $\alpha$, with $\lambda_{\alpha,\,\mathrm{min}} < \lambda < \lambda_{\alpha,\,\mathrm{max}}$, and redshift bin $i$ with $z^i_{\lambda,\,\mathrm{min}} < z < z^i_{\lambda,\,\mathrm{max}}$ is given by

$$
N^i(\lambda_\alpha) = \Omega_s \int_{z^i_{\lambda,\,\mathrm{min}}}^{z^i_{\lambda,\,\mathrm{max}}} \mathrm{d}z\, \frac{\mathrm{d}^2 V}{\mathrm{d}z\mathrm{d}\Omega} \int \mathrm{d}M\, \frac{\mathrm{d}n}{\mathrm{d}M} \int_{\lambda_{\alpha,\,\mathrm{min}}}^{\lambda_{\alpha,\,\mathrm{max}}} \mathrm{d}\ln\lambda\, p(\ln\lambda|M,z),
\tag{20}
$$

where $\mathrm{d}^2 V/\mathrm{d}z\mathrm{d}\Omega$ is the comoving volume element, and $\mathrm{d}n/\mathrm{d}M$ the halo mass function in comoving units for which we omitted the redshift dependence.
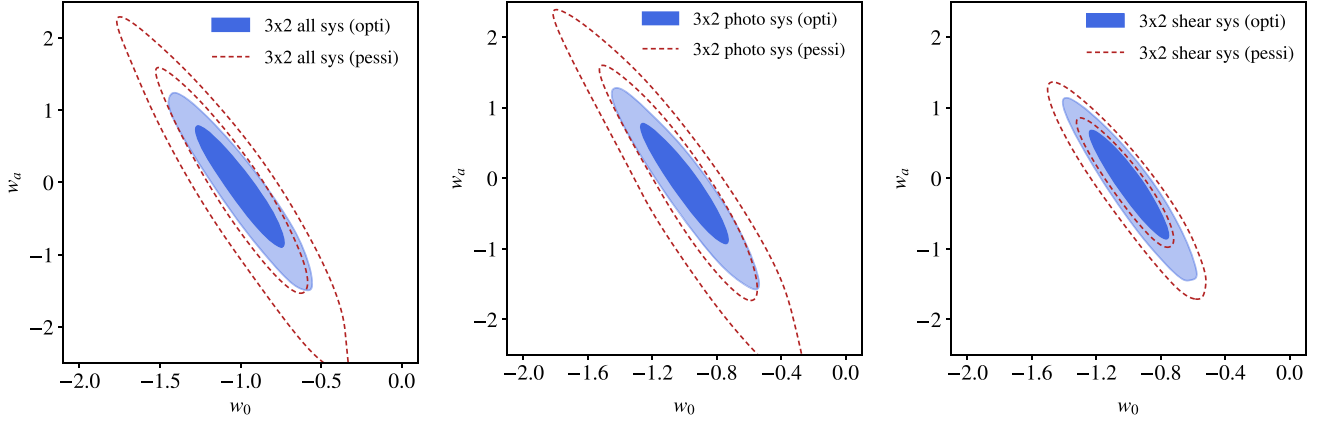
**Figure 6.** Study of systematic effects for a $3\times2$ dark energy analysis. On the very left, we again show Fig. 5 as a baseline. The middle panel shows the difference when only considering photo-$z$ uncertainties, and the right-hand panels show results when only considering shear calibration uncertainties. There are two main findings: (1) In the optimistic scenario, shear calibration and photo-$z$ uncertainties are equally (un)important; and (2) in the pessimistic case, we find that photo-$z$ uncertainties are a significantly larger contribution to the systematics budget compared to shear calibration.

**Table 4.** FoMs for optimistic and pessimistic systematics for shear and photo-$z$ calibration depicted in Fig. 6.

| | Systematics impact FoM summary | |
|---|---|---|
| Systematic | Optimistic | Pessimistic |
| Shear + photo-$z$ | 23.46 | 7.88 |
| Photo-$z$ | 23.56 | 7.00 |
| Shear calibration | 26.95 | 16.88 |

### 4.1.2 Galaxy cluster weak lensing

Starting again from the Limber and flat-sky expression for projected power spectra, i.e. equation (5):

$$C_{AB}^{ij}(l) = \int d\chi \, \frac{q_A^i(\chi) q_B^j(\chi)}{\chi^2} P_{AB}(l/\chi, z(\chi)), \quad (21)$$

we can express the weight function for the projected cluster density similar to equations (6) and (7):

$$q_{\delta_{\lambda_\alpha}}^i(\chi) = \Theta\left(z(\chi) - z_{\lambda,\min}^i\right) \Theta\left(z_{\lambda,\max}^i - z(\chi)\right) \frac{dV}{d\chi \, d\Omega}, \quad (22)$$

with $\Theta(x)$ the Heaviside step function. Note that we neglect variations of the cluster selection function within redshift bins, as well as uncertainties in the cluster redshift estimate.

Within the halo model, the cross-power spectrum between cluster centres and matter density contrast can be written as the usual sum of two- and one-halo term,

$$
\begin{aligned}
P_{\delta_{\lambda_\alpha} m}(k, z) &\approx b_{\lambda_\alpha}(z) P_{\lin}(k, z) \\
&+ \frac{\int dM \frac{dn}{dM} \frac{M}{\bar\rho} \tilde{u}_m(k, M) \int_{\ln\lambda_{\alpha,\min}}^{\ln\lambda_{\alpha,\max}} d\ln\lambda \, p(\ln\lambda|M, z)}{\int dM \frac{dn}{dM} \int_{\ln\lambda_{\alpha,\min}}^{\ln\lambda_{\alpha,\max}} d\ln\lambda \, p(\ln\lambda|M, z)},
\end{aligned}
$$
$$(23)$$

with $P_{\lin}(k, z)$ the linear matter power spectrum. The mean linear bias of clusters in richness bin $\alpha$ reads

$$b_{\lambda_\alpha}(z) = \frac{\int dM \frac{dn}{dM} b_{\rm h}(M) \int_{\ln\lambda_{\alpha,\min}}^{\ln\lambda_{\alpha,\max}} d\ln\lambda \, p(\ln\lambda|M, z)}{\int dM \frac{dn}{dM} \int_{\ln\lambda_{\alpha,\min}}^{\ln\lambda_{\alpha,\max}} d\ln\lambda \, p(\ln\lambda|M, z)}, \quad (24)$$

where $b_{\rm h}(M)$ the halo bias relation, for which we use the fitting function of Tinker et al. (2010). The Fourier transform of the radial

matter density profile within a halo of mass $M$, $\tilde{u}_{\rm m}(k, M)$, is modeled assuming the Navarro–Frenk–White (NFW) profile (Navarro, Frenk & White 1997) with the Bhattacharya et al. (2013) mass–concentration relation $c(M, z)$.

### 4.2 Systematics

#### 4.2.1 Cluster mass–observable relation

We chose to implement the MOR scatter defined in Murata et al. (2018) and further extend their parametrization to account for possible redshift dependence in the scatter of the mass–richness relation.

Specifically, we assume a lognormal distribution with mass- and redshift-dependent mean and scatter $\sigma_{\ln\lambda|M}$:

$$p(\ln\lambda|M, z) = \frac{1}{\sqrt{2\pi}\sigma_{\ln\lambda|M,z}} \exp\left[-\frac{(\ln\lambda - \langle\ln\lambda\rangle(M))^2}{2\sigma_{\ln\lambda|M,z}^2}\right]. \quad (25)$$

The mean relation is defined as

$$\langle\ln\lambda\rangle(M, z|A, B, C) = A + B\ln\left(\frac{M}{M_{\rm pivot}}\right) + C\ln(1 + z), \quad (26)$$

with normalization $A$, slope $B$, redshift dependence $C$, and the pivot mass $M_{\rm pivot} = 3 \times 10^{14}\,\mathrm{M}_\odot\,h^{-1}$. The mass- and redshift-dependent MOR scatter is defined as

$$\sigma_{\ln\lambda|M}(M, z|\sigma_0, q_M, q_z) = \sigma_0 + q_M\ln\left(\frac{M}{M_{\rm pivot}}\right) + q_z\ln(1 + z). \quad (27)$$

We assume fiducial values for $(A, B, \sigma_0, q_M) = (3.207, 0.993, 0.456, 0.0)$, which correspond to the findings in Murata et al. (2018). For the redshift-dependent MOR parameters that are newly introduced in this paper ($C$ and $q_z$) we assume fiducial values of 0.

Our fiducial priors for $\sigma_0$ and $q_M$ are from the posterior distributions derived in Murata et al. (2018), i.e. a Gaussian prior centred at the fiducial values described above and with the width of 0.045 and 0.03, respectively, and a prior for $q_z$ is centred at 0 with the broader width of 0.1.

We note that this is conservative, since prior information on the MOR is expected to grow substantially in the coming years, near-term with the full HSC survey, which will be one of the deepest
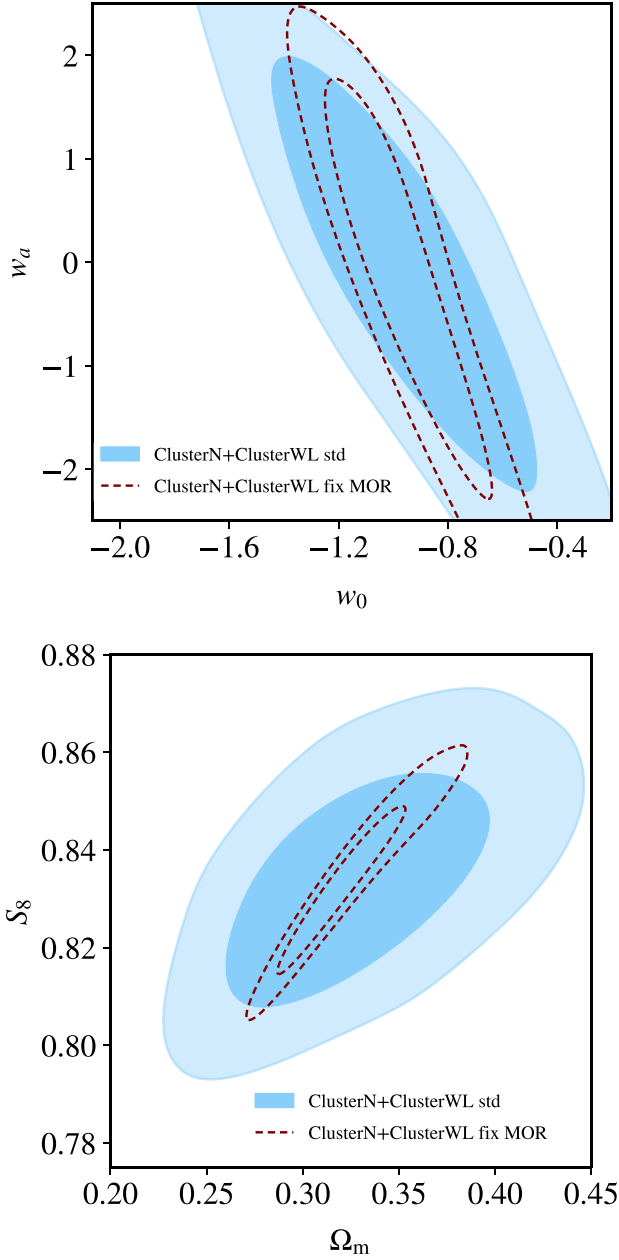
**Figure 7.** Impact on the cosmological constraints from a joint cluster number counts and cluster weak lensing analysis when knowing the MOR perfectly. We show the equation of state parameters $w_0$, $w_a$ (upper panel) and the combination $\Omega_m$ and $S_8 = \sigma_8 \times (\Omega_m/0.315)^{0.35}$ (lower panel).

imaging surveys yielding the most stringent constraints on galaxy cluster physics before the LSST and *Roman Space Telescope* era.

For example, the full HSC survey will have 20 000 optically selected clusters with a mean galaxy density of background sources of 20 arcmin$^{-2}$. Scaling the product of the number of clusters and the source number density in Murata et al. (2018), 8000 clusters and 1 arcmin$^{-2}$, respectively, to the product of these numbers for the full HSC survey translates into a factor of 7 improvement on the priors of the MOR under the assumption that we can translate optical richness as measured in HSC into the realm of NIR *Roman Space Telescope* measurements.

In Fig. 7, we investigate the gain in constraining power for a perfectly known MOR, i.e. when fixing all the parameters in Table 5

**Table 5.** Fiducial parameters, flat priors (min, max), and Gaussian priors centred on the fiducial value with the $\sigma$ given in brackets.

| Parameter | Cluster mass–observable relation scenarios |  |
|---|---|---|
|  | Fiducial | Prior |
| $A$ | 3.207 | Gauss (3.207,0.045) |
| $B$ | 0.993 | Gauss (0.993,0.045) |
| $C$ | 0.0 | Gauss (0.0,0.3) |
| $\sigma_0$ | 0.456 | Gauss (0.456,0.045) |
| $q_M$ | 0.0 | Gauss (0.0,0.03) |
| $q_z$ | 0.0 | Gauss (0.0,0.1) |

to their fiducial values. The gain in information from blue contours to red serves as an upper limit for this particular choice of MOR parametrization. We note that we expected a larger improvement when assuming perfect knowledge of the MOR but we note that the redshift scaling in equation (26) is likely the reason to diminish the science return on dark energy.

Studying the most promising cluster MOR parametrization to optimize the cluster cosmology component of the *Roman Space Telescope* survey further will be important future work as the mission preparation progresses.

### 4.2.2 Other systematics

We note that analyses of cluster number counts and cluster weak lensing of current and future datasets requires the modelling of additional systematic effects, as well as improvements in the ingredients of the forecast model depicted here: For example, we do not consider galaxy cluster mis-centring, assembly bias and stochasticity, cluster member dilution of the source sample, or projection effects in this paper (see, e.g. Oguri & Takada 2011; McClintock et al. 2018). We also point out that both terms in equation (23) need additional modelling as a function of the cluster sample at hand. The two-halo term needs to accurately model halo exclusion (Tinker et al. 2005; García & Rozo 2019), as well as non-linear contributions to halo-matter clustering. For the one-halo term, the NFW profile and Tinker et al. (2010) mass function are likely insufficient and must be calibrated using simulations of the specific cluster sample considered in order to account for e.g. baryonic effects (e.g. Bocquet et al. 2016), halo triaxiality, and scatter in the mass–concentration relation. Implementing a mode detailed cluster cosmology model is beyond the scope of of this paper and we instead postpone studies of these effects to future work.

## 5 THE HIGH LATITUDE SPECTROSCOPIC SURVEY

In this section, we study the trade space of area versus depth for the HLSS, starting from a baseline survey of 2000 deg$^2$ and a wavelength range of 1.05–1.85 $\mu$m. The section is split into two parts, where the first part focuses on dark energy parameter constraints using MCMC and the second part is a Fisher analysis of how well the *Roman Space Telescope* will be able to measure the BAO scale $s$ and the parameter combination $f\sigma_8$ for RSD. The assumptions and systematics modelling differ slightly but are clearly explained in each subsection.

### 5.1 Dark energy forecasts

We use the *Roman Space Telescope* ETC version 16 of Hirata et al. (2012) to compute galaxy densities and redshift distributions for our

**Table 6.** HLSS survey parameters.

| HLSS survey params ($\Omega_s = 2000$ deg$^2$) | | |
|---|---|---|
| Redshift (density weighted) | Comoving volume ($10^9$ Mpc $h^{-1})^3$ | Galaxy density ($h$ Mpc$^{-1})^3$ |
| 0.84 | 2.12 | 0.003 803 |
| 1.28 | 3.23 | 0.002 845 |
| 1.75 | 3.72 | 0.001 182 |
| 2.28 | 3.90 | 0.000 503 |
| 2.75 | 3.87 | 0.000 195 |
| 3.26 | 3.75 | 0.000 069 |
| 3.71 | 2.88 | 0.000 025 |

baseline scenario (cf. Table 6) and then consider doubling (halving) the survey area, doubling (halving) the galaxy number density, and decreasing the minimum scale that we include in our analysis (see Fig. 8).

Following Seo & Eisenstein (2003) and Wang, Chuang & Hirata (2013), we model the cosmological information from RSDs and BAOs through features in the observed power spectrum:

$$P_g(k_\perp^{\mathrm{ref}}, k_\parallel^{\mathrm{ref}}) = \frac{\left[D_A^{\mathrm{ref}}(z)\right]^2 H(z)}{[D_A(z)]^2 H^{\mathrm{ref}}(z)} b^2 \frac{\left(1 + \beta \mu^2\right)^2}{1 + k^2 \mu^2 \sigma_{r,p}^2/2}$$

$$\times \left[\frac{G(z)}{G(z=0)}\right]^2 P_m(k, z=0)\, e^{-k^2 \mu^2 \sigma_{r,z}^2} + P_{\mathrm{shot}}, \quad (28)$$

where we assume that the 3D Fourier mode $k$ can be decomposed into a line-of-sight $k_\parallel$ and a transverse $k_\perp$ component with $\mu = k_\parallel/|k|$ as the cosine of the angle between the 3D vector and the line of sight. The arguments for the observed power spectrum $k_\perp^{\mathrm{ref}}$ and $k_\parallel^{\mathrm{ref}}$ are computed at a reference cosmology, indicated through the superscript $^{\mathrm{ref}}$. The functional form of $H(z)$ and $D_A(z)$ is assumed to be known for any given set of cosmological parameters.

In order to relate the observed power spectrum to the true underlying power spectrum, a correction factor $\left([D_A^{\mathrm{ref}}(z)]^2 H(z)\right) / \left([D_A(z)]^2 H^{\mathrm{ref}}(z)\right)$, which accounts for the volume difference between the two cosmologies, is introduced.

The $1/[1 + k^2 \mu^2 \sigma_{r,p}^2/2]$ term in equation (28) models the small-scale RSD contribution (Wang et al. 2013). It is the Fourier transform of our assumed peculiar velocity distribution,

$$f(v) = \frac{1}{\sigma_p \sqrt{2}} e^{-\sqrt{2}|v|/\sigma_p}, \quad (29)$$

where $\sigma_p$ is the pairwise velocity dispersion that is related to the distance dispersion $\sigma_{r,p}$ as

$$\sigma_{r,p} = \frac{\sigma_p}{H(z)a(z)}. \quad (30)$$

The $P_{\mathrm{shot}}$ term describes residual uncertainties that remain after subtracting the shot noise term computed from the inverse number density of galaxies. These residuals occur, e.g. because of galaxy clustering bias (Seljak 2000). Equation (28) accounts for residual redshift uncertainty in our measurement, e.g. from fitting emission lines, through the damping factor $e^{-k^2 \mu^2 \sigma_{r,z}^2}$. Following Wang et al. (2013), we consider the dewiggeled power spectrum,

$$P_m(k, z=0) = P_0\, k^{n_s}\, T_{\mathrm{dw}}^2(k), \quad (31)$$

where $P_0$ defines the normalization of the linear power spectrum at redshift zero, $n_s$ is the spectral index, and the (dewiggeled) transfer

function $T_{\mathrm{dw}}^2(k, z)$ is given by

$$T_{\mathrm{dw}}^2(k, z) = T_{\mathrm{nw}}^2(k) + \left[T^2(k) - T_{\mathrm{nw}}^2(k)\right] e^{-g_\mu k^2/(2k_*^2)}$$

$$\equiv T_{\mathrm{nw}}^2(k) + T_{\mathrm{BAO}}^2(k) e^{-g_\mu k^2/(2k_*^2)}, \quad (32)$$

where $g_\mu(k, z) = 1 - \mu^2 + \mu^2[(1 + f_g(z))^2 - 1]$ (cf. Eisenstein, Seo & White 2007) and $f_g(z)$ being the linear growth factor.

The BAO transfer function is defined as the difference between the linear matter transfer functions with and without baryons, and the exponential damping due to non-linear effects is only applied to the transfer function associated with BAO. The uncertainty in non-linear effects that are still present in the power spectrum even after reconstruction (Seo & Eisenstein 2007; Padmanabhan et al. 2012) is paramtrized through

$$k_*^{-1} = 8.355\, \mathrm{Mpc}\, h^{-1}\, \frac{\sigma_8}{0.8}\, p_{\mathrm{NL}}. \quad (33)$$

In case no reconstruction algorithm is applied, non-linear effects in structure growth, galaxy bias, and redshift-space distortions are fully present and $p_{\mathrm{NL}} = 1.0$. We assume an optimistic reconstruction algorithm in line with Wang et al. (2013) of $p_{\mathrm{NL}} = 0.5$, which corresponds to $k_* = 0.24h\, \mathrm{Mpc}^{-1}$. We allow for uncertainty in the reconstruction algorithm through varying $k_*$ and marginalize over a Gaussian prior with 10 per cent uncertainty in the fiducial value.

The dewiggled model characterized through equation (32) will break down on small scales where RSD couples with the damping factor but has been shown to work well on quasi-linear scales (Angulo et al. 2008).

We bin the observable power spectrum linearly in $k$ (100 bins between $k_{\mathrm{min}} = 0.001$ and $k_{\mathrm{max}} = 0.3$) and $\mu$ (10 bins between 0 and 1) and assume seven bins in redshift (cf. Table 6). We model the fractional error of said power spectrum as detailed in Seo & Eisenstein (2003):

$$\sigma(k, \mu) = 2\pi \sqrt{\frac{2}{V_{\mathrm{survey}} k^2 \Delta k \Delta \mu}} \left(\frac{1 + n P(k, \mu)}{n}\right), \quad (34)$$

where $n$ refers to the galaxy number density within a given redshift bin, which again are specified in Table 6.

Fig. 8 shows the variation of the *Roman Space Telescope* and BAO and RSD measurements on $w_0$ and $w_a$. We again use the EMCEE sampler to cover the parameter space; each chain is >3M steps and, in addition to the cosmological parameters mentioned in Table 2, we sample the 11 systematics parameters specified in Table 7. Specifically, we account for uncertainties in the level of shot noise $P_{\mathrm{shot}}$ (one parameter), uncertainties in galaxy bias modelling parametrized through one free parameter $b_i$ in each redshift bin (seven parameters), uncertainties in redshift measurements $\sigma_{r,z}^2$ (one parameter), uncertainties in modelling peculiar velocities $\sigma_p$ in each redshift bin (seven parameters), and uncertainty in residual non-linear effects $k_*$ (one parameter).

Fig. 8 shows the change in constraining power when increasing/decreasing the survey area (left-hand panels), increasing/decreasing the number density of galaxies (middle panel) and when changing our fiducial $k_{\mathrm{max}}$ from 0.3 to 0.25 and 0.2. Note that the observing time is not held fixed in the left-hand and middle panels (as opposed to the calculations in Section 5.2), which means that when considering twice the area in the left-hand panels this implies doubling the observing time compared to reference HLSS survey. We summarize the FoMs in Table 8 and find that the difference for different $k_{\mathrm{max}}$ is negligible, and that there is a slight preference for going deeper compared to going wider.
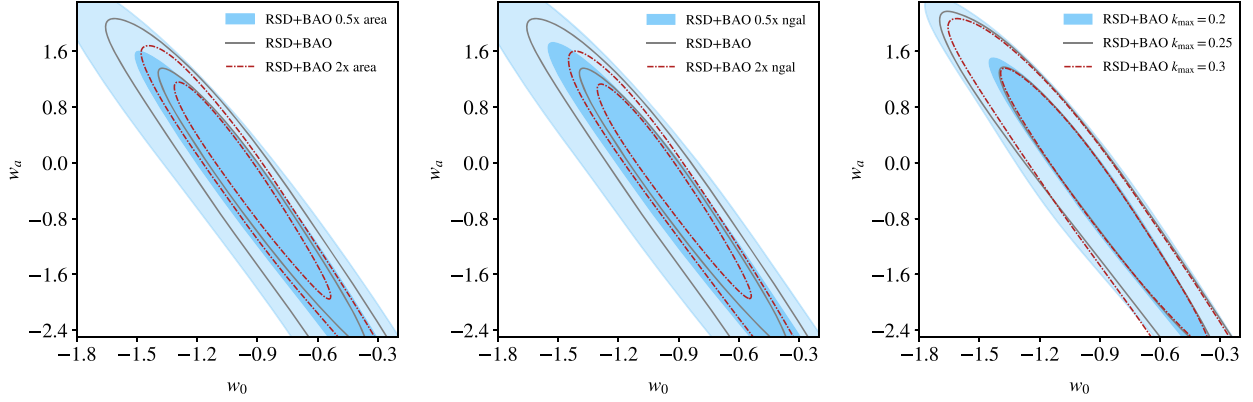
**Figure 8.** The impact of variations in area, depth, and scales to which we assume to be able to model $P_\delta(k)$ for the HLSS part of the reference survey (0.6 months). We summarize the FoMs in Table 8.

**Table 7.** Spectroscopic Survey: fiducial parameters, flat priors (min, max), and Gaussian priors centred on the fiducial value with the $\sigma$ given in brackets.

| | HLSS systematics parameters | |
| --- | --- | --- |
| Parameter | Fiducial | Prior |
| $b_1$ | 1.55 | [0.6-4.2] |
| $b_2$ | 1.87 | [0.6-4.2] |
| $b_3$ | 2.22 | [0.6-4.2] |
| $b_4$ | 2.62 | [0.6-4.2] |
| $b_5$ | 2.97 | [0.6-4.2] |
| $b_6$ | 3.38 | [0.6-4.2] |
| $b_7$ | 3.72 | [0.6-4.2] |
| $\sigma_p(i)$ | $290\,\mathrm{km\,s}^{-1}$ | Gaussian (290, 50) |
| $k_*$ | $0.24\,h\,\mathrm{Mpc}^{-1}$ | Gaussian (0.24, 0.024) |
| $\sigma_{r,z}$ | 0.001 | Gaussian (0.001,0.0001) |
| $P_\mathrm{shot}$ | 0.0 | [−0.001,0.001] |

**Table 8.** FoM for chains depicted in Fig. 8.

| | HLSS FoM summary | | |
| --- | --- | --- | --- |
| Area | $2000\,\mathrm{deg}^2$ | $4000\,\mathrm{deg}^2$ | $1000\,\mathrm{deg}^2$ |
| FoM | 8.19 | 14.34 | 5.33 |
| Galaxy density | Reference | $2 \times$ ref | $0.5 \times$ ref |
| FoM | 8.19 | 14.60 | 4.74 |
| $k_\mathrm{max}$ | 0.3 | 0.25 | 0.2 |
| FoM | 8.19 | 7.79 | 6.68 |

We note that including an absolute measurement of the BAO scale imprinted in the CMB would notably increase the information compared to the HLSS survey alone. In Fig. 9, we include information from (Planck Collaboration VI 2018) on the acoustic angular scale $\theta_* = r_*/(1 + z)D_a$, where $r_*$ is the comoving sound horizon at recombination and $D_a$ is the comoving angular diameter distance to the CMB. The combined likelihood of Planck TT, TE, EE, low-E measurements gives $\theta_* = 0.010\,4109 \pm 0.000\,0030$, which we re-centre to our fiducial cosmology and use as a prior in Fig. 9.

**5.2 BAO scale and RSD measurement Fisher forecasts**

In addition to the MCMC analysis in the previous subsection, we explore the science return of the HLSS using a Fisher analysis on
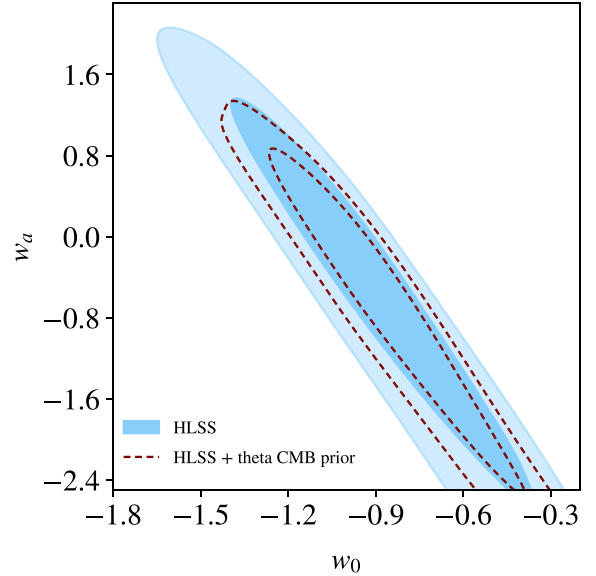


**Figure 9.** We see the gain in constraining power when assuming that the scale of the BAO feature in the CMB is known at Planck precision (see equation 9 in Planck Collaboration VI 2018).

constraining the BAO scale $s$ and RSD parameter combination $f\sigma_8$ as a function of redshift.

For this analysis we run the ETC in BAO survey mode, using either galaxies observed in H$\alpha$ and [N II] (compilation option -N II) or in [O III] (-DOIII_GAL) as tracers. For the H$\alpha$ and [N III] detections, we use model option 992, an average of the three galaxy luminosity functions given in Pozzetti et al. (2016), which were derived specifically for *Euclid* and the *Roman Space Telescope*; in all cases, the [N II] luminosity function (used to enhance the S/N of detected galaxies) is assumed to be 0.37 times the H$\alpha$ luminosity function. For the [O III] detections, we use model 1992, an average of three luminosity functions: Mehta et al. (2015) and Colbert et al. (2013), two different analyses of the WFC3 grism, and Khostovan et al. (2015), based on ground-based narrow-band surveys. In both the H$\alpha$ + [N II] and [O III] scenarios, we use an updated galaxy size distribution from a mock catalogue based on COSMOS data originally based on Jouvel et al. (2009).
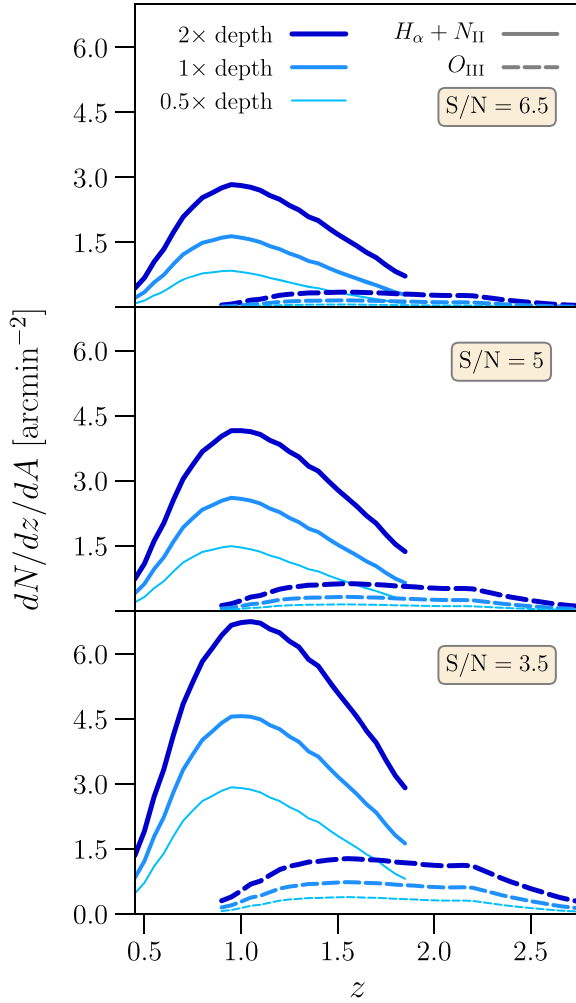
**Figure 10.** d$N$/d$z$/d$A$ for the two galaxy populations used in the BAO and RSD forecast: H$\alpha$ + [N II] (solid lines) and [O III] (dashed lines). The various curves used in the trade-off study are shown: (1) from the top to bottom panel, varying the S/N cutoff from 6.5, 5, to 3.5; (2) inside each panel, varying survey depth from 2×, 1×, to 0.5× the fiducial depth with decreasing thickness. These curves are used as input for the forecast results shown in Fig. 11.

The resulting redshift distributions are shown in Fig. 10, which are used as input for the trade-off studies of the forecast results in this section. In each panel, we vary the survey depth from 0.5×, 1×, to 2× the fiducial depth (shown in thick, normal, and thin lines, respectively), while the different panels show the distributions obtained with different S/N cutoffs (6.5, 5, and 3.5). As expected, the number densities increase significantly when lower S/N cutoffs are chosen. Note that in this section, we explore the impact of survey depth at fixed observation time, so the area of the survey is scaled proportionally in what follows.

Using each of the above-mentioned distributions, we compute the fractional error $\sigma_{p_i}/p_i = [F^{-1}]_{ii}$ on parameter $p_i$, where the Fisher information matrix for parameters $p_i$ and $p_j$ is given by

$$F_{ij} = \int_{k_{\min}}^{k_{\max}} \frac{\partial \ln P_g(\mathbf{k})}{\partial p_i} \frac{\partial \ln P_g(\mathbf{k})}{\partial p_j} V_{\text{eff}}(\mathbf{k}) \frac{\mathrm{d}\mathbf{k}^3}{2\,(2\pi)^3}, \qquad (35)$$

assuming spatially constant galaxy density $n$, we have

$$V_{\text{eff}}(k, \mu) = \left[ \frac{n P_g(k, \mu)}{n P_g(k, \mu) + 1} \right]^2 V_{\text{survey}}. \qquad (36)$$

There are two separate Fisher matrices, one for the RSD cosntraints on $f\sigma_8$, and another for the BAO constraints on $s$. For the RSD constraint, we follow McDonald & Seljak (2009) (using only one tracer) and model the observed galaxy power spectrum as in equation (28) but without the distance ratios for changing cosmology as we fix the background cosmology:

$$P_g(k_\perp^{\text{ref}}, k_\parallel^{\text{ref}}) = b^2 \left( 1 + \beta\,\mu^2 \right)^2$$
$$\times \left[ \frac{G(z)}{G(z=0)} \right]^2 P_m(k, z=0) \mathrm{e}^{-k^2 \mu^2 \sigma_{r,z}^2} + P_{\text{shot}}. \qquad (37)$$

and we marginalize over $\sigma_{r,z} = \sigma_{r,v}(1 + z)/H(z)$. We adopt the fiducial value of $\sigma_{r,v} = 0.001$, which is dominated by the observational redshift uncertainty of the grism. Furthermore, for the RSD forecast, we assume perfect reconstruction with $k_* = \infty$.

For the BAO constraints, we calculate errors for the Hubble parameter $H$ and the angular diameter distance $D$ and report their best constrained combination $s$. Again we use equation (35) but this time, modelling the galaxy power spectrum as defined in equation (37) with the following differences: First, the fractional reconstruction capability $p_{\text{NL}}$ is set by how well the displacements can be determined, given the level of shot noise in the data in linear theory. Secondly, $\sigma_{r,z}$ is not marginalized for the BAO forecast but is fixed at the same fiducial value mentioned above.

For both BAO and RSD forecasts, we use the inverse galaxy number density for the galaxy shot noise, and the same linear bias model as in DESI Collaboration et al. (2016) for emission-line galaxies (ELGs) as is appropriate for the *Roman Space Telescope* GRS: $b_{\text{ELG}}(z)D(z) = 0.84$, where $D(z)$ is the growth factor normalized at $z = 0$.

The Fisher matrices are computed at a fixed flat cosmology consistent with Planck 2015 best fit (baseline model 2.6; Ade et al. 2016) and we separately evaluate fractional errors on parameters for the H$\alpha$ + [N II] and [O III] samples before inverse-variance combining them. In Fig. 11 we show the combined fractional error on the BAO scale $s$ (left-hand panels) and RSD parameter $f\sigma_8$ (right-hand panels). Note that the H$\alpha$ is the dominant sample up to $z \approx 1.9$, beyond which the [O III] sample becomes the only available sample.

We consider different survey strategies varying depth (top row of Fig. 11) and S/N (middle row) starting from a pilot survey with default area $A = 2000\ \text{deg}^2$ and S/N cutoff 5. We fix the total HLSS observation time to 0.6 yr in all cases. In the top panels, we show results for a deeper (twice deeper, half the area) and a wider survey (twice the area, half the depth) compared to the pilot survey. For both $s$ and $f\sigma_8$, the wide survey would improve the low-$z$ constraints, whereas the deep survey is more powerful at higher $z$, as expected.

Since the aggregate constraint (shown in the text beside each curve) is dominated by better errors at low-$z$, the wide survey would improve on the total constraint on parameters compared to the deep survey (e.g. 0.3 per cent versus 0.4 per cent for $s$ and 0.7 per cent versus 1.1 per cent for $f\sigma_8$). On the other hand, if dark energy behaviour at higher $z$ becomes an important science case, the deep survey improves constraining power by almost a factor of 2–3 over the wide option.

In the middle row of Fig. 11, we also show the impact of different S/N cutoffs for galaxy detections at fixed area and depth. We compare our default case of S/N = 5 with a conservative S/N = 6.5, and a more optimistic S/N cutoff of 3.5. As expected, a lower S/N cutoff yields
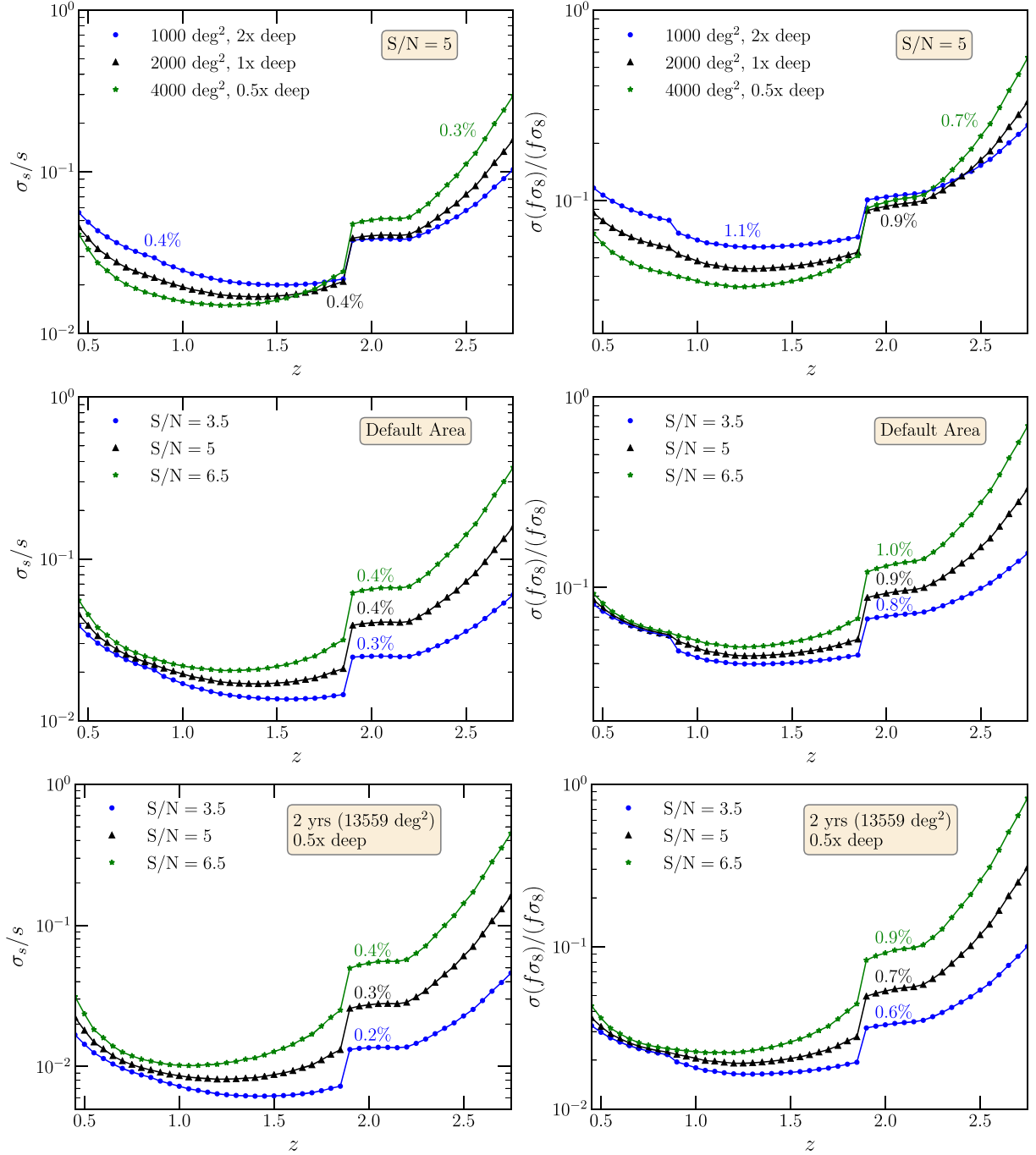
**Figure 11.** For all rows in this plot, we show the fractional error on the BAO scale (left-hand panels) and the error on the RSD parameter combination $f\sigma_8$ (right-hand panels) at a redshift binwidth of $dz = 0.05$. The aggregate fractional error over the entire redshift range is indicated near each curve. Upper row shows the results for a 0.6-yr HLSS survey of $H\alpha + $ [N II] and [O III] galaxies; varying area and depth for a fixed default S/N cutoff of 5. The default scenario (black) has $A = 2000$ deg$^2$, the wide scenario (green) has twice the area but half the depth, whereas the deep scenario (blue) is twice deeper but half the area. For both the BAO and RSD probes, a wider but shallower survey improves the constraints for $z \lesssim 2$ whereas a deeper but narrower survey improves at $z \gtrsim 2$. The middle row shows results when varying the S/N cutoff (3.5, 5, 6.5) for the default area and depth scenario. A lower S/N cutoff yields better constraints everywhere in $z$, with more improvement at higher $z$. The bottom row shows results when covering a larger area of 13 559 deg$^2$ corresponding to an extended spectroscopic survey time of 2 yr at half the default depth. We vary again the S/N cutoff: 3.5, 5, and 6.5.

better constraints everywhere in $z$, with more improvement at higher $z$ as fainter and distant galaxies are more affected by the cut. There is factor of 2 improvement at high $z$ between the curves at S/N = 6.5 and 5. The same is true for 5 and 3.5; we however note that S/N = 3.5 is not likely going to be a realistic value for reliable detections.

We perform a similar analysis but for an extended HLSS survey that lasts 2 yr instead of 0.6 yr and at only half the depth of the pilot survey, which allows us to survey 13 559 deg$^2$ (see the bottom row of Fig. 11). We show results for three different S/N cut and again find unsurprisingly that an S/N cut of 3.5 improves constraining

power substantially compared to the more realistic S/N = 5 and the conservative S/N = 6.5 cuts.

# 6 CONCLUSIONS

The *Roman Space Telescope*'s wide-field instrument will join the concert of cosmological endeavors after DESI, LSST, SPHEREx, and Euclid have already made initial measurements. These measurements will inform the design of an optimal *Roman Space Telescope* survey, which can be finalized shortly before launch. The unique versatility of its wide-field instrument, ranging from multiband imaging to high-resolution slitless spectroscopy, in combination with the fact that the *Roman Space Telescope* carries enough propellant for at least 10 yr of observations with no active cryogens, make it an ideal observatory to flexibly target the most interesting science aspects after its launch in the mid-2020s.

In this paper, we study the *Roman Space Telescope* reference survey's science return on dark energy, structure growth, and modified gravity accounting for a variety of observational systematics. We present results for the joint analysis of weak lensing, galaxy clustering (photometric), galaxy cluster number counts, BAO and RSD features in the spectroscopic clustering power spectrum, and combine this with SN Ia information from the *Roman Space Telescope* (as detailed in Hounsell et al. 2018). We outline strategies for optimizing the *Roman Space Telescope*'s science return and to identify and retire risks from systematic effects early.

For each cosmological probe examined in this paper, we identify important areas of future research to further increase the level of realism of our *Roman Space Telescope* simulations, to improve the parametrization of systematics, or to shrink the prior range on existing parametrizations. For example, we postpone modelling and mitigation of baryons (e.g. van Daalen et al. 2011; Eifler et al. 2015; Chisari et al. 2018; Chisari et al. 2019; Huang et al. 2019) or intrinsic galaxy alignment (e.g. Hirata & Seljak 2004; Mandelbaum et al. 2006; Joachimi & Bridle 2010; Krause et al. 2016; Blazek et al. 2019; Samuroff et al. 2019; Vlah et al. 2019) for lensing-based measurements to future studies, a decision that is in part driven by the fact that these uncertainties have different levels of modelling maturity for the different probes considered in this paper. We explore corresponding uncertainties in a companion paper (Eifler et al. 2020), which focusses on 3×2 (weak lensing and photometric galaxy clustering) synergies of the *Roman Space Telescope* and LSST.

We impose conservative scale cuts on photometric clustering information due to uncertainties in modelling galaxy bias. Improved galaxy bias modelling for the spectroscopic and photometric galaxy clustering to include small scale information (see e.g. Ivanov, Simonović & Zaldarriaga 2019; Salcedo et al. 2020; Wibking et al. 2020) should become another important area for *Roman Space Telescope* optimization. Krause & Eifler (2017) have explored a Halo Occupation Density model to access small scale information in a similarly high-dimensional parameter space (but simulating an LSST 3×2 analysis), and found that tapping into corresponding information is worth the increased modelling complexity.

Our modelling of the cluster MOR is based on Murata et al. (2018) but extended to account for possible redshift dependence in the scatter of the mass–richness relation. This again is a conservative choice and tightening priors on the existing parametrization or improving the parametrization itself can significantly change the constraining power from galaxy clusters. Precise modelling of cluster cosmology is an active research field (e.g. see Costanzi et al. 2019; DES Collaboration et al. 2020) and studying multiwavelength strategies including external data sets will be important.

We quantify all statements in this paper using the well-known FoM metric; however, we note that the FoM metric reduces a complex answer to a one-dimensional statement. This compression of information is not lossless; for example, the FoM depends on analysis choices: scales considered and excluded in the analysis, redshift distribution binning choices, cosmological parameters and priors, systematics parametrization and priors, which covariance and cross-correlations to include, and how to model the covariance in general, which external data sets to include, are all choices by the analyst. Multiple options are justifiable and for some the impact on the FoM can be significant.

While the decision on the optimal *Roman Space Telescope* survey strategy can be made shortly before launch, it is critical to develop realistic survey simulation capabilities now in order to characterize the trade space of statistical power and systematic dangers accurately. Some of these systematics will have subdominant uncertainties, which means they can be corrected and need no further parametrization in a likelihood analysis. This type of systematics will hardly change the error bars presented in this paper; it will only move the best-fitting value in a likelihood analysis based on data.

It is important to note that complexity of modelling and covariance code such as the one used in this paper will become a challenge for the community. Increased complexity in a prediction and later in an analysis framework does not automatically increase the precision but it certainly increases the potential for errors. Increased model complexity for systematics must to be rigorously justified by residual uncertainties that are non-negligible, given the constraining power of the survey. This requires a demonstration of the impact of the systematic effect in the presence of a realistic systematics budget overall; it is not sufficient to demonstrate the impact of the systematic as a standalone effect on cosmological parameters.

This work contributes to developing such a framework for the *Roman Space Telescope*, but several extensions are forthcoming in future work. More realistic systematics models, best informed by actual observations and realistic synergy studies across the whole spectrum of multimessenger astronomy, which includes optical NIR imaging and spectroscopy but also CMB, gravitational waves, and radio observations, should be considered to design a survey that fully utilize the *Roman Space Telescope*'s potential.

## DATA AVAILABILITY

The data underlying this paper will be shared on reasonable request to the corresponding author.

# REFERENCES

Abazajian K. N. et al., 2016, preprint (arXiv:1610.02743)
Ade P. A. R. et al., 2016, A&A, 594, A13
Ade P. et al., 2019, J. Cosmol. Astropart. Phys., 2019, 056
Angulo R. E., Baugh C. M., Frenk C. S., Lacey C. G., 2008, MNRAS, 383, 755
Bernstein G. M., Jarvis M., 2002, AJ, 123, 583
Bhattacharya S., Habib S., Heitmann K., Vikhlinin A., 2013, ApJ, 766, 32
Blazek J., Vlah Z., Seljak U., 2015, J. Cosmol. Astropart. Phys., 8, 015
Blazek J. A., MacCrann N., Troxel M. A., Fang X., 2019, Phys. Rev. D, 100, 103506
Bocquet S., Saro A., Dolag K., Mohr J. J., 2016, MNRAS, 456, 2361
Chisari N. et al., 2015, MNRAS, 454, 2736
Chisari N. E. et al., 2018, MNRAS, 480, 3962
Chisari N. E. et al., 2019, Open J. Astrophys., 2, 4
Colbert J. W. et al., 2013, ApJ, 779, 34
Costanzi M. et al., 2019, MNRAS, 488, 4779
de Jong R. S., 2019, Nat. Astron., 3, 574
DES Collaboration et al., 2020, Phys. Rev. D, 102, 023509
DESI Collaboration et al., 2016, preprint (arXiv:1611.00036)
Dodelson S., Schneider M. D., 2013, Phys. Rev. D, 88, 063537
Doré O. et al., 2014, preprint (arXiv:1412.4872)
Eifler T., Krause E., Dodelson S., Zentner A. R., Hearin A. P., Gnedin N. Y., 2015, MNRAS, 454, 2451
Eifler T. F., Simet M., Krause E., Hirata C., Huang H., 2021, MNRAS, preprint (arXiv:2004.04702)
Einstein A., 1917, Kosmologische Betrachtungen zur allgemeinen Relativitätstheorie, Sitzungsberichte der Königlich Preußischen Akademie der Wissenschaften, Berlin
Eisenstein D. J., Seo H.-J., White M., 2007, ApJ, 664, 660
Fang X., Krause E., Eifler T., MacCrann N., 2019, J. Cosmol. Astropart. Phys., 05, 010
Foreman-Mackey D., Hogg D. W., Lang D., Goodman J., 2013, PASP, 125, 306
García R., Rozo E., 2019, MNRAS, 489, 4170
Goodman J., Weare J., 2010, Commun. Appl. Math. Comput. Sci., 5, 65
Grogin N. A. et al., 2011, ApJS, 197, 35
Hemmati S. et al., 2019, ApJ, 877, 117
Hirata C. M., Seljak U., 2004, Phys. Rev. D, 70, 063526
Hirata C. M., Gehrels N., Kneib J.-P., Kruk J., Rhodes J., Wang Y., Zoubian J., 2012, preprint (arXiv:1204.5151)
Hounsell R. et al., 2018, ApJ, 867, 23
Huang H.-J., Eifler T., Mandelbaum R., Dodelson S., 2019, MNRAS, 488, 1652
Ivanov M. M., Simonović M., Zaldarriaga M., 2019, J. Cosmol. Astropart. Phys., 05, 042
Ivezić Ž. et al., 2019, ApJ, 873, 111
Joachimi B., Bridle S. L., 2010, A&A, 523, A1
Jouvel S. et al., 2009, A&A, 504, 359
Khostovan A. A., Sobral D., Mobasher B., Best P. N., Smail I., Stott J. P., Hemmati S., Nayyeri H., 2015, MNRAS, 452, 3948
Koekemoer A. M. et al., 2011, ApJS, 197, 36
Krause E., Eifler T., 2017, MNRAS, 470, 2100

Krause E., Eifler T., Blazek J., 2016, MNRAS, 456, 207
Laureijs R. et al., 2011, preprint (arXiv:1110.3193)
McClintock T. et al., 2018, MNRAS, 482, 1352
McDonald P., Seljak U., 2009, J. Cosmol. Astropart. Phys., 2009, 007
Mandelbaum R., Hirata C. M., Ishak M., Seljak U., Brinkmann J., 2006, MNRAS, 367, 611
Mehta V. et al., 2015, ApJ, 811, 141
Murata R., Nishimichi T., Takada M., Miyatake H., Shirasaki M., More S., Takahashi R., Osato K., 2018, ApJ, 854, 120
Navarro J. F., Frenk C. S., White S. D. M., 1997, ApJ, 490, 493
Oguri M., Takada M., 2011, Phys. Rev. D, 83, 023008
Padmanabhan N., Xu X., Eisenstein D. J., Scalzo R., Cuesta A. J., Mehta K. T., Kazin E., 2012, MNRAS, 427, 2132
Perlmutter S. et al., 1999, ApJ, 517, 565
Planck Collaboration et al., 2018, A&A, 641, 67
Pozzetti L. et al., 2016, A&A, 590, A3
Riess A. G. et al., 1998, AJ, 116, 1009
Salcedo A. N., Wibking B. D., Weinberg D. H., Wu H.-Y., Ferrer D., Eisenstein D., Pinto P., 2020, MNRAS, 491, 3061
Samuroff S. et al., 2019, MNRAS, 489, 5453
Schaan E., Krause E., Eifler T., Doré O., Miyatake H., Rhodes J., Spergel D. N., 2017, Phys. Rev. D, 95, 123512
Seljak U., 2000, MNRAS, 318, 203
Semboloni E., Hoekstra H., Schaye J., van Daalen M. P., McCarthy I. G., 2011, MNRAS, 417, 2020
Seo H.-J., Eisenstein D. J., 2003, ApJ, 598, 720
Seo H.-J., Eisenstein D. J., 2007, ApJ, 665, 14
Simpson F. et al., 2013, MNRAS, 429, 2249
Singh S., Mandelbaum R., More S., 2015, MNRAS, 450, 2195
Spergel D. et al., 2015, preprint (arXiv:1503.03757)
Takada M. et al., 2014, PASJ, 66, R1
Takahashi R., Sato M., Nishimichi T., Taruya A., Oguri M., 2012, ApJ, 761, 152
Taylor A., Joachimi B., Kitching T., 2013, MNRAS, 432, 1928
Tenneti A., Singh S., Mandelbaum R., Matteo T. D., Feng Y., Khandai N., 2015, MNRAS, 448, 3522
Tinker J. L., Weinberg D. H., Zheng Z., Zehavi I., 2005, ApJ, 631, 41
Tinker J. L., Robertson B. E., Kravtsov A. V., Klypin A., Warren M. S., Yepes G., Gottlöber S., 2010, ApJ, 724, 878
Troxel M. A., Ishak M., 2014, Phys. Rep., 558, 1
van Daalen M. P., Schaye J., Booth C. M., Dalla Vecchia C., 2011, MNRAS, 415, 3649
Vlah Z., Chisari N. E., Schmidt F., 2019, J. Cosmol. Astropart. Phys., 01, 025
Wang Y., Chuang C.-H., Hirata C. M., 2013, MNRAS, 430, 2446
Wibking B. D., Weinberg D. H., Salcedo A. N., Wu H.-Y., Singh S., Rodríguez-Torres S., Garrison L. H., Eisenstein D. J., 2020, MNRAS, 492, 2872
Zentner A. R., Semboloni E., Dodelson S., Eifler T., Krause E., Hearin A. P., 2013, Phys. Rev. D, 87, 043509

This paper has been typeset from a TEX/LATEX file prepared by the author.